Petrological constraints on melt generation beneath the Asal Rift (Djibouti) using quaternary basalts

Paul Pinzuti, Eric Mercier, Isabelle Manighetti, Yves Gaudemer

Geochemistry Geophysics Geosystems G3

Article
Volume 14, Number 8
22 August 2013
doi: 10.1002/ggge.20187
ISSN: 1525-2027

Published by AGU and the Geochemical Society

Petrological constraints on melt generation beneath the Asal Rift (Djibouti) using quaternary basalts

Paul Pinzuti and Eric Humler
Laboratoire de Planétologie et Géodynamique de Nantes, UMR 6112, 2 rue de la Houssinière BP 92208, FR-44322, Nantes Cedex 3, France (paulpinzuti@gmail.com)

Isabelle Manighetti
Géoazur, UMR6526, Valbonne, France

Yves Gaudemer
Laboratoire de Tectonique et Mécanique de la Lithosphère, UMR 7154, Institut de Physique du Globe de Paris, Université Paris VII, France

[1] The temporal evolution of the mantle melting processes in the Asal Rift is evaluated from the chemical composition of 56 new lava flows sampled along 10 km of the rift axis and 9 km off-axis (i.e., erupted within the last 620 kyr). Petrological and primary geochemical results show that most of the samples of the inner floor of the Asal Rift are affected by plagioclase accumulation. Trace element ratios and major element compositions corrected for mineral accumulation and crystallization show a symmetric pattern relative to the rift axis and preserved a clear signal of mantle melting depth variations. While FeO, $Fe_{8.0}$, Zr/Y, and $(Dy/Yb)_N$ decrease from the rift shoulders to the rift axis, SiO_2, Na/Ti, Lu/Hf increase and Na_2O and $Na_{8.0}$ are constant across the rift. These variations are qualitatively consistent with shallow melting beneath the rift axis and deeper melting for off-axis lava flows. $Na_{8.0}$ and $Fe_{8.0}$ contents show that beneath the rift axis, melting paths are shallow, from 81 ± 4 to 43 ± 5 km. These melting paths are consistent with adiabatic melting in normal-temperature fertile asthenosphere, beneath an extensively thinned mantle lithosphere. On the contrary, melting on the rift shoulders (from 107 ± 7 to 67 ± 8 km) occurred beneath thicker lithosphere, requiring a mantle solidus temperature 100 ± 40°C hotter. In this geodynamic environment, the calculated rate of lithospheric thinning appears to be 4.0 ± 2.0 cm yr^{-1}, a value close to the mean spreading rate (2.9 ± 0.2 cm yr^{-1}) over the last 620 kyr.

Components: 9,154 words, 9 figures, 2 tables.

Keywords: geochemistry; petrology; continental breakup; rifting; Asal Rift.

Index Terms: 1700 History of Geophysics; 1749 Volcanology, geochemistry, and petrology; 1000 Geochemistry; 1065 Major and trace element geochemistry; 1032 Mid-oceanic ridge processes; 3600 Mineralogy and Petrology; 3614 Mid-oceanic ridge processes; 8400 Volcanology; 8416 Mid-oceanic ridge processes; 4825 Geochemistry.

Received 22 March 2013; **Revised** 22 May 2013; **Accepted** 24 May 2013; **Published** 22 August 2013.

Pinzuti, P., E. Humler, I. Manighetti, and Y. Gaudemer (2013), Petrological constraints on melt generation beneath the Asal Rift (Djibouti) using quaternary basalts, *Geochem. Geophys. Geosyst., 14*, 2932–2953, doi:10.1002/ggge.20187.

1. Introduction

[2] From continental rifting to seafloor spreading, the continental crust is progressively modified by magmatism. Although substantial progress has been made on petrology and geochemistry of continental basalts [e.g., *Fram et al*., 1998; *DePaolo and Daley*, 2000; *Wang et al*., 2002], the temperature and pressure conditions of melting that lead to magmatism during this process are still poorly constrained [e.g., *Bastow and Keir*, 2011]. The reasons are that the genesis and evolution of continental basalts are due to many other factors, which can be difficult to decipher. For example, crustal contributions may partially or completely mask the composition of magma that is formed in the mantle [e.g., *Glazner et al*., 1991; *Glazner and Farmer*, 1992] and even without crustal contamination, there is a debate concerning the role of mantle plume [e.g., *Bradshaw et al*., 1993; *Parsons et al*., 1994] and lithospheric versus asthenospheric mantle in the basalt genesis [e.g., *Dungan et al*., 1986; *Kempton et al*, 1991; *DePaolo and Daley*, 2000]. Moreover, because of the absence of glasses and the rarity of aphyric rock samples, it is also necessary to use whole rock data. The problem is that the presence in the whole-rock of phenocrysts that are out of equilibrium with their host melt modifies the chemical composition of samples and lead to uncertainty in the interpretation of the major elements.

[3] The East African Rift System is a classic example of continental breakup, where the deformation of the continental crust is located along magmatic segments [e.g., *Manighetti et al*., 1998; *Manighetti et al*., 2001; *Doubre et al*., 2007a, 2007b; *Ebinger et al*., 2008; *Ferguson et al*., 2013]. The central Main Ethiopian Rift marks the transition between rifting of thick continental crust in the southern and central East African Rift System and incipient seafloor spreading in the northern Afar, into the Afar Depression [e.g., *Hayward and Ebinger*, 1996; *Rooney et al*., 2007]. The broad range of lithologies for potential crustal assimilants has prompted the application of multiple petrographic and geochemical (e.g., Ce/Pb, Ti/Yb, K/P, La/Nb, Sr, Nd, Hf, and Pb isotopes) indicators of crustal contamination. For instance, the relationships between Sr-Nd isotopic ratios and K/P and Ti/Yb ratios have been used to assess the role of crustal contamination in lavas from the Afar depression [*Deniel et al*.,1994; *Barrat et al*., 1990; *Vigier et al*., 1999; *Hart et al*. 1989; *Schilling et al*., 1992; *Rooney et al*., 2012a]. Most of the analyzed basalts have low K/P ratios (<5) and there are no correlations between these ratios and the Sr and Nd isotopic ratios suggesting the absence of significant silicic crustal contamination. Furthermore, the contribution of the upper mantle asthenosphere (mid-ocean ridge basalt (MORB)-like source) is best recognized in the young lavas (<4 Ma), particularly in the Tadjoura area and the Asal Rift (3–0 Ma), where Hf-Pb data have affinity to, and overlap with, the East Sheba Ridge (Aden Ridge) data and has Indian Ocean-like Hf and Pb isotope signatures [*Rooney et al*., 2012a]. However it has been shown that these lava flows exhibit values consistent with mixing between Afar plume and regional lithospheric mantle [*Schilling et al*., 1992; *Rooney et al*., 2012a, *Rooney et al*., 2013].

[4] These geochemical data suggest that the major element composition of the recent basalts (<1 Ma) from the Gulf of Tadjoura and the Asal Rift can be used confidently to constrain mantle melting processes.

[5] As shown elsewhere [e.g., *Klein and Langmuir*, 1987; *Klein and Langmuir*, 1989; *Langmuir et al*., 1992; *Lee et al*., 2009], major element data can be quantitatively linked to the extent of melting (F_{mean}), the initial and final pressures of melting (P_0 and P_f), mantle temperature and crustal thickness (h_c). For instance, increasing F_{mean} has the main effect of lowering Na_2O in the melt (Na_2O behaves as an incompatible element during mantle melting). FeO varies largely as a function of P_0 with relatively small variations as a function of F. Thus, Na and Fe contents of the mantle melts provide constraints on the final depth of melting P_f (from Na_2O, which reflects F_{mean} and therefore P_0-P_f), on the initial depth of melting (P_0) and thus, on the solidus temperature (from FeO). The petrologically constrained crustal thickness can

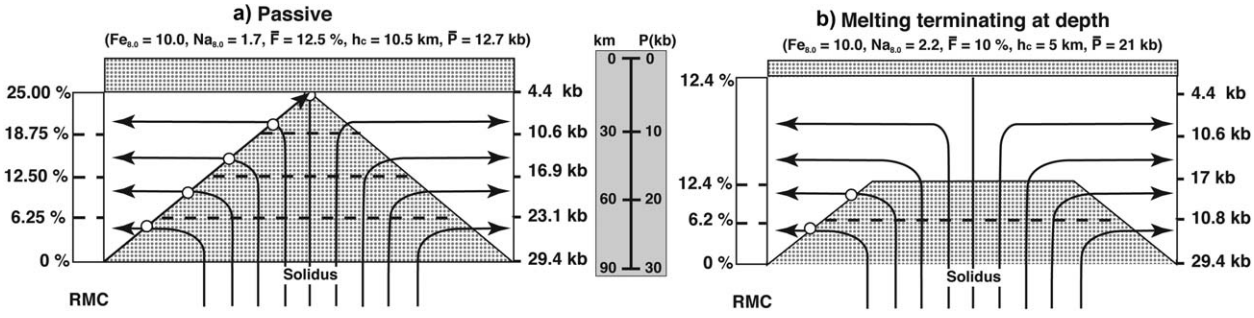

Figure 1. Models for passive (standard model) and melting terminating at depth (modified from *Langmuir et al*. [1992]). All melting regimes are drawn to scale, where 1 kbar is equal to 3 km of mantle or 3.3 km of crust, and is 1.2% $kbar^{-1}$. The mean properties of the steady state ocean crust generated by each melting regime are given, and may be calculated from residual mantle column (RMC). F_{mean}: with mean in subscript characters is the mean extent of melting, P_{mean}: with mean in subscript characters. is the mean pressure of melting, h_c is crustal thickness, and F_{max} is the maximum amount of melting in the melting regime. (a) The passive model is for equilibrium melting and complete melt focusing. (b) The melting regime beneath thick lithosphere is compressed by a freezing front. FeO corrected for fractional crystallization at 8% MgO ($Fe_{8.0}$) is identical in both cases (10%) but because the melting column is shorter in melting regime terminating at depth, the $Na_{8.0}$ content is larger (2.2%) compared to the standard model (1.7%). Indeed, the petrologically constrained crustal thickness is thicker in the standard case (10.5 km) relative to the melting regime ceasing at depth (5 km).

be then compared to geophysical observations and the mantle flow regime can be determined (standard model versus melting terminating at depth for instance). In Figure 1, FeO corrected for fractional crystallization at 8% MgO ($Fe_{8.0}$) is identical in both cases (10%) but because the melting column is shorter in the melting regime terminating at depth, the $Na_{8.0}$ content is larger (2.2%) compared to the standard model (1.7%). Indeed, the petrologically constrained crustal thickness is thicker in the standard case (10.5 km) relative to the melting regime ceasing at depth (5 km).

[6] The present study focuses on the conditions of melting that lead to magmatism during continental rifting through the example of the Asal Rift. Our study area covers 12 km of the rift (Figure 2), out of 9 km from the axis (that is to an equivalent age of about 620 kyr). Spatial petrological and geochemical studies of the rift, which is easily accessible to field observations, give us the opportunity to constrain the magmatic evolution during the rifting process based on 56 new lava flows sampled in this area. The key questions we try to solve are as follows: How large are mantle temperature variations beneath the rift and at what depth does the mantle cease to melt? Which melting conditions are required to fit both petrological and geophysical data using a "normal" mantle composition? These constrains are useful to illustrate the mantle thermal state beneath a newly fragmented continent.

[7] In the following, we will first use major element composition of basalts corrected for mineral accumulation and for crystallization to estimate the temporal variations of the initial and final pressures and temperatures of melting. Subsequently, trace elements ratios insensitive to phenocrysts accumulation and crystallization are used to test the results obtained from the major element approach. Finally, we propose a "petrologically constrained lithospheric thickness" and deduce the rate of lithospheric thinning in the studied area.

2. Geological and Geophysical Constraints

[8] The Afar depression is a unique area where the transition between continental and oceanic rifting is working and observable. This area is stretched by the separation of the Africa and Arabia plate, whose boundaries correspond to the Aden and Red Sea Ridge (Figure 2a). The Africa-Arabia separation was initiated 30 Myr ago [e.g., *Hofmann et al*., 1997; *Courtillot et al*., 1999] by the activity of a mantle plume leading to intraplate volcanism [e.g., *Schilling*, 1973; *White and McKenzie*, 1989; *Marty et al*., 1993; *Deniel et al*., 1994; *Courtillot et al*., 1999]. The Afar area is characterized by active rifting taking place along several disconnected rift segments propagating on land (Figure 2a) [e.g., *Varet and Gasse*, 1978; *Courtillot*, 1980; *Manighetti et al*., 1998].

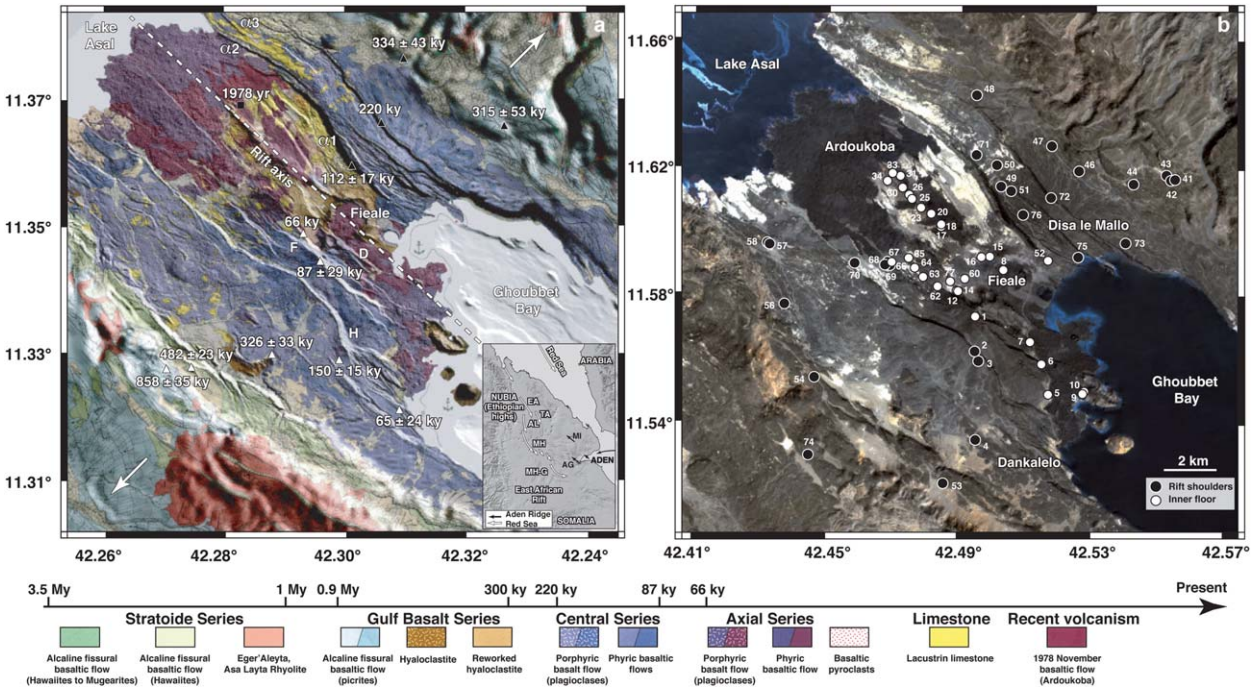

Figure 2. (a) Geological map of the emerged part of the Asal Rift [*Stieltjes*, 1980] combined to IGN, ASTER, and SRTM DEM. K/Ar ages of basaltic lava flows are from *Manighetti et al*. [1998]. Letters correspond to the name of the major border faults from *Manighetti et al*. [2001]. Inset shows regional tectonic settings where the arrows represent the rift segments and indicate the direction of propagation: MI, Manda Inakir; AG, Asal-Ghoubbet; T, Tadjoura; EA, Erta Ale; TA, Tat'Ali; AL, Alayta; MH, Manda Hararo; MH-G, Manda Hararo-Goba'ad. Modified from *Manighetti et al*. [2001]. (b) Sample location across the Asal Rift. Black and white dots, respectively, correspond to the samples collected on the shoulders and on the inner floor of the rift.

[9] The Asal Rift (Figure 2) is the first emergent segment of the Aden Ridge, which propagates westward on land into the Afar depression (Figure 2a) [*Manighetti et al*., 1998]. With a ~40 km length, whose 15 km are emerged between the Ghoubbet Bay and Lake Asal, it currently opens at 1.6 ± 0.1 cm yr^{-1} in the N40° ± 5°E direction (Figure 2) [*Ruegg and Kasser*, 1987; *Vigny et al*., 2007]. The Asal Rift evolution starts after the injection of rhyolitic domes through NW-SE faults, around 1 Ma. This silicic volcanism can be related to the emplacement of the Aden Ridge propagator [*Lahitte et al*., 2003]. Around 852 ± 85 kyr, the rhyolite domes were covered by the Gulf basalts series (Figure 2a), which have been interpreted as deriving from fissural eruptions associated with incipient rifting [*Richard*, 1979]. These Gulf basalts series started to erupt 853 ± 35 kyr and ended with a hyaloclastite eruption episode 326 ± 15 kyr ago (Figure 2a). On either side of the Asal Rift, the youngest basalts of theses series are bound or offset by faults, which delimit the Central series (Figure 2a). This magmatic episode filled the rift between 300 and 50 kyr from a central volcano, the Fieale [*Manighetti et al*., 1998]. Whereas basaltic flows older than 150 ± 15 kyr have apparently spread astride the rift zone, flows younger than 87 ± 29 kyr abut fault scarps and therefore tend to have concentrated near the rift axis [*De Chabalier and Avouac*, 1994]. After 90 kyr, magmatic activity decreased and border faults, which are currently observed, started to grow. The geometry of the modern rift began with the development of normal faults on either side of the new inner floor [*Manighetti et al*., 1998; *Pinzuti et al*., 2010]. Later, the axial series erupted from small volcanic edifices aligned along eruptive fissures in the inner floor. The latest volcanic event occurred at the northwestern tip of the volcanic ridge in 1978 (Ardoukoba volcano, Figures 2a and 2b).

[10] Mechanical stretching models [e.g., [*Dunbar and Sawyer*, 1989; *Lin and Parmentier*, 1990] have been previously proposed to explain the long-term evolution of the Asal Rift. However, recent study [*Pinzuti et al*., 2010] shows that this evolution could be related to localized magma intrusion at depth.

While the crustal thickness outside of the Asal Rift is about 20–25 km [*Hammond et al*. 2011], deep seismic sounding [*Ruegg*, 1975] and others geophysical approaches give crustal thickness beneath the rift of ~5 km [*Tarantola et al*., 1980; *Lépine and Hirn*, 1992; *De Chabalier and Avouac*, 1994; *Doubre et al*., 2007a, 2007b], the first 500 m near the rift axis corresponding to the basalts flooded since ~1 Myr [*Demange and Puvilland*, 1993].

[11] Deep structure of the Afar depression is constrained by seismic refraction and seismological data [*Ruegg*, 1975; *Berckhemer et al*, 1975; *Makris and Ginsburg*, 1987; *Knox et al*, 1998; *Nyblade et al*, 2000; *Rychert et al*. 2012]. *Knox and et al*. [1998] localized a pronounced negative *S* wave velocity gradient beneath Afar Depression between 60 and 110 km, which is characteristic of the upper mantle. From seismic refraction studies, *Ruegg* [1975] estimates that the lithosphere-astenosphere boundary at the both side of the Aden Ridge is located to a depth of 58 km and rises up to 45 km at 100 km of ridge axis (profiles 01 and 06).

3. Data Acquisition and Laboratory Work

3.1. Chemical Analyses

[12] We sampled 56 new basaltic lava flows across the Asal Rift during a field trip organized in 2000. The major and trace element compositions of each sample (Tables SI1–SI4) were measured from small volume of rock (~few cm^3), which were preliminarily powdered using agate mortar and 90° alcohol. The major element compositions were measured by Inductively Coupled Plasma Atomic Emission Spectrometer and the trace elements were determined by Inductively Coupled Plasma Mass Spectrometry at Centre de Recherches Pétrographiques et Géochimiques (CRPG-CNRS Nancy-France). Measurement uncertainties are: $Al_2O_3 < 1\%$, $SiO_2 < 1\%$, $FeO < 2\%$, $MgO < 2\%$, $CaO < 2\%$, $Na_2O < 5\%$, $TiO_2 < 5\%$, $P_2O_5 < 10\%$, $K_2O < 2\%$, $MnO < 5\%$, and $< 5\%$ for trace elements.

[13] To observe detailed mineral assemblages from microscope, we make thin sections of samples at the Laboratoire de Planétologie and Géodynamique de Nantes (France). From 12 of these thin sections, we analyzed the major chemical composition of mineral phenocrysts from Microprobe (CAMECA SX 100) at the Institut de Physique du Globe de Paris-CAMPARIS (France). Average major chemical composition of groundmass of six samples were also analyzed from Scanning Electron Microspcopy (SEM) (JEOL 7600F and JEOL 5800LV) at the Institut des Matériaux Jean Rouxel (Nantes, France). All mineralogical descriptions are given in the supporting information (see Figures SI1–SI38 and Tables SI5–SI8).[1]

3.2. Mineral Accumulation Correction

[14] Because a large part of the Asal Rift samples is affected by mineral accumulation, we corrected the whole-rock composition of the samples from modal abundances and chemical composition of phenocryst phases using simple mass balance calculations. We used two different procedures based on modal analysis and phase identification, both from digital photographs and scanned images of thin section. These quantitative modal analyses are based on the calculation of the area occupied by individual minerals on an image, groundmass and porosity normalized to the total thin section area. The main assumption of these approaches is that the mineral abundance is related to the percentage of the area it occupies, assuming that there is a direct relation with the volume percent [e.g., *Petruk*, 1989].

[15] The first procedure is based on the analyses of 20 thin sections using a binocular polarizing microscope combined with a CANON EOS 350D. For each thin section, we realized a mozaic of pictures under plane-polarized light (Figures SI1–SI38), using Autopanogiga© software. In this configuration, the color of olivine and clinopyroxene is light brown, iron and titan oxides are black, but unfortunately, plagioclases and vesicles filled of resin appear white. Consequently, to separate these two phases, we also realized five mozaics for each thin section in cross polarized from a series of pictures taken every 30°, from 0° to 150°. Using image2003© software [*Launeau and Robin*, 1996], we then applied to each set of mozaic a Fourier series decomposition to extract an ellipse from the second optical component. The result corresponds to an image, where each mineral phase has a maximum intensity and the vesicles always appear black.

[16] From the plane-polarized light and Fourier panoramas, it is then straightforward to select and assign to each phase a separate color combining them in one over layer using Image2003 and/or Adobe Photoshop CS3© software. From the final

[1] Additional supporting information may be found in the online version of this article.

mineral maps, a first abundance of each phase is estimated as the ratio of the pixel number of the assigned color divided by the size of the picture in pixels, using Image2003 software. At last, the final mineral abundance of each mineral phase (Tables SI1 and SI2) is calculated by normalizing the first estimation by the porosity.

[17] The remaining dataset was analyzed using scanned images of thin section from Epson Expression 10,000XL scanner. Each thin section was scanned as negative film, first under naturel light, and second between two polarizing films. Mappings of the thin sections were realized from this couple of scanned images. The main difference with the first approach is that the phenocrysts presented on the polarized images do not show maximum intensity. Consequently, to clearly separate plagioclases and porosity filled of resin, it is sometimes necessary to verify the mapping of the thin section with a binocular polarizing microscope. The procedure is less convenient than the first one, but is still faster because several thin sections can be scanned together.

4. Age/Distance Relationship in the Asal Rift

[18] Since this study deals with temporal variation of basalts chemistry, we need to check precisely the relationship between geochronological ages of samples and their distances to the active rift axis. In order to test this relationship, we used K-Ar age (Figure 2a) published in *Manighetti et al*. [1998]. K-Ar age (Figure 2a) versus distance to the rift axis for 10 flows from the northern and southern shoulders of the Asal Rift is plotted in Figure SI39 (see supporting information). The distances from the rift axis are calculated from the projection of the sample location along the N43°E direction (Figures 2 and SI39). This direction is consistent with the azimuth opening direction of the Asal Rift and corresponds to the perpendicular of the rift axis, which is defined as the line passing through the caldera of the Fieale volcano and through the axial volcanic chains located in the central part of the inner floor (Figure 2a).

[19] The linear correlation between K-Ar ages and distance to the axial rift [e.g., *De Chabalier and Avouac*, 1994; *Ferguson et al*., 2013] defines a mean spreading rate of 2.9 ± 0.2 cm yr^{-1}. However, anomalous young age for one sample outside the rift indicate an off-axis volcanism on the northern shoulder and suggest that eruptions occurred 66 kyr ago within a zone 3 km wide (subrift Dankalelo, Figures 2a and 2b) [*Manighetti et al*., 1998]. If this data set is statistically significant for the studied area, we can use the distance of samples to the rift axis as a proxy for their geochronological ages. The calculated extension rate (2.9 ± 0.2 cm yr^{-1}) is higher than the current value obtained from Global Positioning System measurements (1.6 ± 0.1 cm yr^{-1}) [*Ruegg and Kasser*, 1987; *Vigny et al*., 2007] but is close to the long-term spreading rate for the studied area [*De Chabalier and Avouac*, 1994]. In the following, the data are projected along the line perpendicular to the rift axis (distance of samples from the rift axis and calculated ages are related by Distance = 29 Age, with distance in km and ages in kyr (Table 1). We organized the samples in two groups, from the rift axis distance. The first group corresponds to the samples from the Gulf Basalt and Central series (group B), and the second one includes the samples from the axial series, which characterized the inner floor of the Asal Rift (group A). This inner floor is delimitated by the Southern (faults H, F, D) and Northern (faults α1, α2, α3) border fault systems (Figure 2a). Its width ranges from ~2 km at the Fieale caldera to more than 5 km near the Lake Asal (Figure 2). For our study, we used a mean width of 4100 m, which is the best estimate that characterized most of the samples from the axial series (Figure 2).

5. Evidence for Plagioclase Accumulation

5.1. Petrological Observations

[20] Petrological analysis shows that most of the Asal Rift lava flows correspond to high vesicular basalts. Most samples of the rift shoulders (~64%) have an aphyric texture. The majority of the lava flows of the inner floor (~75%) correspond to porphyritic basalts with plagioclase megacrysts (~8% to ~54%), olivine (~0.1% to ~6%) and clinopyroxene (~5%) in lesser proportion. Microprobe analyses reveal that the majority of these mineral phases have a close chemical composition from one sample to the other one (Tables SI5–SI7).

[21] The plagioclase megacrysts correspond to Bytownite (An_{76-88}; Table SI5) with a size that can reach 1 cm (Figure SI40A), which is unusual in eruptive rocks. A few part of plagioclase crystals are subeuhedral, but the majority of them

Table 1. Compositional Parameters, Calculated Pressure, and Depth of Melting for the Basalts of the Asal Rift Corrected for Mineral Accumulation[a]

Sample ID	Longitude (°)	Latitude (°)	Distance (m)	Location	$Fe_{8.0}^*$ (%)	$Na_{8.0}^*$ (%)	Zr/Y	Na^*/Ti^*	$(Dy/Yb)_N$	Lu/Hf	P_o (kbar)	P_f (kbar)	F_{mean} (%)	D_c (km)	D_l (km)	D_m (km)
AF01	42.4945	11.5751	1357	A	8.91	2.54	5.159	2.776	1.326	0.120	23.75	12.65	10	3.77	38.88	73.06
AF05	42.5158	11.5527	1614	A	8.88	2.42	4.527	3.543	1.254	0.135	23.59	10.94	11	4.52	34.67	72.35
AF06	42.5142	11.5601	1129	A	8.36	2.60	4.554	3.235	1.243	0.134	20.53	8.80	10	3.87	28.20	63.05
AF07	42.5091	11.5671	933	A	8.80	2.10	4.809	2.745	1.326	0.125	23.37	5.14	12	7.61	15.94	55.51
AF08	42.5024	11.5887	335	A	9.30	2.32	4.892	2.787	1.279	0.123	26.07	13.36	11	4.75	41.73	80.00
AF10	42.5272	11.5536	700	A	9.79	2.51	5.084	2.768	1.291	0.116	28.97	18.27	10	3.67	56.65	89.13
AF12	42.4885	11.5834	1122	A	8.96	2.29	4.870	3.124	1.338	0.121	24.08	10.20	11	5.26	32.12	73.82
AF14	42.4885	11.5834	1122	A	10.16	2.22	4.491	3.248	1.311	0.134	31.15	17.91	12	5.19	54.95	95.81
AF15	42.4982	11.5928	360	A	10.2	2.48	4.427	3.888	1.265	0.133	31.38	20.53	10	3.77	63.83	96.31
AF16	42.4957	11.5927	168	A	9.46	2.21	4.674	2.759	1.358	0.123	27.08	13.29	12	5.43	40.81	83.20
AF17	42.4839	11.6012	8	A	9.97	2.39	4.269	3.708	1.270	0.149	30.02	18.27	11	4.25	56.73	92.20
AF18	42.4839	11.6023	81	A	8.88	2.24	4.379	3.913	1.288	0.135	23.64	8.86	12	5.75	26.55	72.50
AF20	42.4815	11.6046	92	A	9.45	2.30	4.870	2.948	1.287	0.125	26.98	14.13	11	4.86	44.16	82.75
AF23	42.4777	11.6069	0	A	9.49	2.12	4.544	3.553	1.268	0.132	27.26	12.22	12	6.21	37.28	83.76
AF25	42.4764	11.6089	57	A	9.87	2.41	4.342	3.464	1.257	0.149	29.45	17.79	11	4.19	55.17	90.52
AF26	42.4764	11.6089	67	A	8.96	2.32	4.336	3.486	1.270	0.138	24.10	10.54	11	5.08	33.16	73.90
AF30	42.4732	11.6127	142	A	9.12	2.34	4.146	3.645	1.304	0.141	25.06	12.32	11	4.72	38.23	76.97
AF31	42.4718	11.6160	308	A	10.19	2.62	4.689	3.142	1.271	0.132	31.34	21.59	10	3.20	66.97	96.36
AF33	42.4708	11.6166	283	A	9.83	2.46	4.742	2.981	1.266	0.129	29.21	18.02	10	3.93	55.83	89.84
AF34	42.4697	11.6163	177	A	8.96	2.04	4.604	3.377	1.281	0.133	24.24	5.66	13	8.00	17.54	56.60
AF52	42.5157	11.5907	1479	A	10.86	2.39	4.657	2.319	1.400	0.112	35.26	23.55	11	4.24	72.77	108.42
AF60	42.4920	11.5847	758	A	9.23	2.45	4.934	2.700	1.270	0.123	25.66	14.30	11	4.01	44.52	78.85
AF62	42.4828	11.5819	1665	A	9.24	2.02	4.732	2.577	1.349	0.119	26.02	5.79	13	8.80	22.11	79.53
AF63	42.4771	11.5862	1734	A	9.53	2.41	4.706	2.750	1.259	0.126	27.46	15.86	11	4.16	49.48	84.34
AF64	42.4750	11.5890	1660	A	9.18	2.52	4.369	3.140	1.234	0.136	25.39	14.82	10	3.61	46.07	78.08
AF65	42.4733	11.5920	1541	A	9.37	2.26	4.160	3.940	1.263	0.143	26.51	13.11	12	5.17	40.87	81.32
AF66	42.4682	11.5906	2031	A	8.96	2.31	4.444	3.474	1.279	0.136	24.08	10.37	11	5.16	32.65	73.85
AF77	42.4868	11.5858	1051	A	9.44	2.42	4.986	2.664	1.287	0.121	26.88	15.41	11	4.10	47.95	82.62
Mean				A	**9.41 ± 0.21**	**2.35 ± 0.06**	**4.62 ± 0.10**	**3.16 ± 0.20**	**1.29 ± 0.01**	**0.13 ± 0.00**						
AF02	42.4941	11.5651	2203	B	10.91	2.22	4.871	2.106	1.440	0.113	35.68	22.41	12	5.21	68.95	109.80
AF03	42.4952	11.5623	2350	B	9.80	1.92	4.784	2.073	1.406	0.114	29.52	10.30	14	8.81	34.22	90.27
AF04	42.4945	11.5391	4295	B	10.27	2.49	5.274	2.377	1.352	0.111	31.83	20.97	10	3.77	65.19	97.70
AF41	42.5518	11.6154	6156	B	10.40	2.31	5.301	2.631	1.416	0.108	32.61	20.25	11	4.64	62.79	100.13
AF42	42.5518	11.6154	6156	B	10.86	2.48	5.291	2.913	1.430	0.107	35.28	24.29	10	3.83	75.36	108.32
AF43	42.5506	11.6167	6173	B	11.27	2.44	5.415	2.768	1.420	0.105	37.69	26.34	11	4.02	81.42	115.86
AF44	42.5407	11.6141	5231	B	12.26	2.56	5.886	2.367	1.445	0.101	43.52	33.06	10	3.52	101.90	133.80
AF46	42.5243	11.6178	4324	B	10.18	2.23	5.710	2.671	1.384	0.111	31.29	18.11	12	5.15	55.60	96.24
AF47	42.5168	11.6250	4359	B	11.34	2.48	5.623	2.644	1.381	0.106	38.11	27.12	10	3.82	83.85	117.13
AF48	42.4940	11.6398	3886	B	10.47	2.32	5.693	2.596	1.413	0.105	33.03	20.74	11	4.60	64.22	101.51
AF49	42.5016	11.6132	2276	B	11.33	2.27	5.580	2.419	1.426	0.106	38.14	25.36	11	4.90	78.33	117.20
AF50	42.5002	11.6195	2687	B	10.06	2.24	5.661	2.667	1.401	0.108	30.56	17.41	12	5.12	53.76	93.89
AF51	42.5045	11.6119	2383	B	10.59	2.04	5.605	2.451	1.530	0.111	34.08	18.12	13	6.87	56.93	104.26
AF53	42.4850	11.5267	6007	B	11.97	2.48	5.528	2.411	1.338	0.110	41.79	30.79	10	3.82	95.06	128.46
AF54	42.4466	11.5574	6333	B	12.22	2.30	5.486	2.243	1.364	0.108	43.61	30.73	11	4.87	94.83	133.84
AF56	42.4376	11.5786	5266	B	11.60	2.34	5.089	2.659	1.425	0.111	39.67	27.49	11	4.52	84.57	122.19
AF57	42.4326	11.5966	4165	B	11.27	2.25	5.398	2.664	1.416	0.110	37.78	24.83	12	5.00	76.76	116.05
AF58	42.4326	11.5966	4165	B	10.99	2.24	5.588	2.688	1.416	0.109	36.12	23.06	12	5.09	71.02	111.14

Table 1. (continued)

Sample ID	Longitude (°)	Latitude (°)	Distance (m)	Location	$Fe_{8.0}$* (%)	$Na_{8.0}$* (%)	Zr/Y	Na^*/Ti^*	$(Dy/Yb)_N$	Lu/Hf	P_o (kbar)	P_f (kbar)	F_{mean} (%)	D_c (km)	D_l (km)	D_m (km)
AF67	42.4679	11.5906	2053	B	8.68	2.43	4.600	3.267	1.296	0.135	22.40	9.17	11	4.71	29.52	68.66
AF68	42.4679	11.5906	2053	B	10.76	1.97	4.577	1.875	1.428	0.115	35.35	18.05	13	7.74	57.48	107.71
AF69	42.4679	11.5906	2053	B	10.97	2.12	4.593	1.997	1.457	0.107	36.17	21.64	12	6.00	67.09	110.88
AF70	42.4583	11.5907	2752	B	11.17	2.31	5.221	2.379	1.407	0.111	37.14	24.82	11	4.63	76.70	114.15
AF71	42.4943	11.6222	2472	B	9.75	2.35	4.241	3.058	1.295	0.137	28.77	16.56	11	4.51	51.40	88.42
AF72	42.5160	11.6100	3076	B	9.27	2.18	5.762	2.855	1.379	0.104	25.95	11.49	12	5.79	35.44	79.64
AF73	42.5385	11.5950	3511	B	9.42	2.15	5.716	2.770	1.408	0.105	26.85	12.28	12	5.92	37.22	82.57
AF74	42.4450	11.5348	8295	B	11.98	2.56	5.788	2.706	1.465	0.096	41.85	31.44	10	3.50	97.07	128.67
AF75	42.5244	11.5923	2251	B	11.6	2.41	4.634	2.179	1.422	0.115	39.67	28.10	11	4.15	86.54	122.13
AF76	42.5080	11.6050	2078	B	9.75	2.16	5.450	2.752	1.379	0.108	28.76	14.75	12	5.66	45.67	88.31
Mean				**B**	**10.75 ± 0.35**	**2.29 ± 0.06**	**5.30 ± 0.17**	**2.54 ± 0.12**	**1.40 ± 0.02**	**0.11 ± 0.00**						

[a] $Fe_{8.0}$* and $Na_{8.0}$* values correspond to FeO and Na_2O corrected to 8 % MgO. $(Dy/Yb)_N$ ratios are normalized to chondritic values from *Sun and McDonough* [1989]. A: Samples from the inner floor of the Asal Rift; B: Samples from the shoulders of the Asal rift; Distance (m): distance of samples from the rift axis. P_o: initial pressure; P_f: final pressure; F_{mean} (%) : mean extent of melting; D_c: thickness of the basaltic crust; D_l: thickness of the lithosphere; D_m: depth of the residual mantle base.

display melt inclusions, anhedral outlines or corroded boundaries (Figures SI40A–SI40C).

[22] Olivine (Fo_{60-80}; Table SI6) and clinopyroxene (Di_{40-42} En_{26-30} Fs_{6-9}; Table SI7) are minor or absent in most of the basalt of the Asal Rift, and the mean size of these minerals is smaller than those of plagioclase (~0.3 to ~6 mm). In the same thin section, few of these minerals are subeuhedral, but most of them are anhedral (Figure SI40D), also showing fractures, and corrosion dissolution forms (Figures SI40E and SI40F). The three phases can also presents mineral inclusions, and grains attached together or to the rims of other mineral phases (Figures SI40A and SI40G–SI40J).

[23] Groundmass (Figures SI40K–SI40L) consists of plagioclase laths (An_{60-72}; Table SI8), olivine (Fo_{53-66}; Table SI8), clinopyroxene microlites (Di_{32-38} En_{18-26} Fs_{8-12}; Table SI8) and remote opaque oxides (Table 8). As megacrysts, microprobe and SEM analyses reveal that the majority of the mineral phases have an equivalent chemical composition from a sample to the other, but these compositions are slightly different than those of the large size minerals (Tables SI5–SI7).

[24] As shown previously for the basalts of the Asal Rift [*Bizouard et al.*, 1980; *Vigier et al.*, 1999], these petrological characteristics suggest that the three phases are issued from a complex thermal evolution. The homogeneity of the chemical composition of the Bytownite megacrysts (An_{76-88}; Table SI5) implies constant high temperatures (>1200°C) over a long time period [*Clocchiatti et al.*, 1978; *Bizouard et al.*, 1980]. Petrological observations and microprobe analyses also reveal that the megacrysts are clearly out of equilibrium with the groundmass and show that most of the Asal Rift basalts correspond to cumulate rocks. Due to the large proportion of bytownite, which is able to float free of a denser mafic melt, the mineral accumulation credibly occurs at the roof of the magma chamber [*Bizouard et al.*, 1980].

5.2. Major and Trace Element Variations Across the Asal Rift

[25] The chemical variations of the major element across the Asal Rift for all basalts younger than 620 kyr (that is 9 km from the rift axis) are reported in Figure SI41 and Tables SI1 and SI2 (see supporting information). Al_2O_3 and CaO show clear trends, increasing from the rift

shoulders to the rift axis. Inverse trends are observed for MgO and FeO (Figure SI41).

[26] However, we note a large chemical variability for samples within the rift relative to those sampled on the rift shoulders. Asal Rift basalts do not show simple relationships in binary diagrams (Figure SI42). For MgO = 6%, Al_2O_3 varies from ~14 to ~22% and FeO between ~6% and ~15%. Recent differentiated lava flows (low MgO) composition are Al_2O_3 rich and thus do not fit the classical petrological trend. Increasing Al_2O_3, CaO, and decreasing SiO_2, FeO, with decreasing MgO reflect plagioclase accumulation. The presence of phenocrysts in whole rocks drastically modifies the major chemical compositions of the samples. Trace element contents (Tables SI3 and SI4) are also sensitive to the presence of plagioclase in whole rocks, as shown by the positive Eu anomaly of the Rare Earth Elements (REE) patterns of the rift shoulders and the inner floor basalts (Figure 3). The high CaO (~14%) and Al_2O_3 (~24%) contents suggest the presence of cumulative plagioclase. Eu/Eu^* ratios of 1–1.3 (Tables SI1and SI2) confirm these observations and indicate that plagioclase accumulation occurred in most of the samples. Figure SI43 shows that the Sr/Sm ratios positively correlate with Al_2O_3 content. The trend can be reproduced by the addition of variable proportions of plagioclases (Sr and Al_2O_3 rich and Sm poor) to an aphyric basalt with a low Sr/Sm ratios and Al_2O_3 content (41 and 14%, respectively).

[27] Major and trace element composition and petrological analysis reveal that most of the basalts of the Asal Rift are affected by plagioclase accumulation (and to a lesser extent by olivine and clinopyroxene), which leads to uncertainty in the interpretation of the chemical composition. In the following section, we thus correct the whole-rock chemical composition of each sample from the chemical composition and the abundance of phenocrysts.

5.3. Results of the Mineral Accumulation Correction

[28] The chemical variations due to the plagioclase accumulation are illustrated in Figure 4, where the relationship between the plagioclase abundance and Al_2O_3, CaO, FeO, and SiO_2 contents is compared in binary diagrams. This figure shows a linear relationship between the plagioclase abundance and major chemical composition of the samples. The more the proportion of the plagioclase increases, the more the chemical composition of the samples is shifted toward the chemical composition of Bytownite. Thus, the increase of Al_2O_3 and CaO and the decrease of FeO and SiO_2 contents, revealed in the binary diagrams, are clearly explained by the addition of plagioclase to magmas.

[29] From the abundance and the chemical composition of the mineral phases, we corrected the whole rock major element composition for phenocryst accumulation using equation (2) (see supporting information). The major chemical composition of the mineral phases is based on the average of several core mineral microprobe analyses (Tables SI5–SI7) realized from 12 samples. In the following, major elements contents corrected for mineral accumulation are denoted by asterisks (Tables SI9 and SI10). Figure SI44 shows a clear linear relationship between the corrected whole rock major element composition estimated from the mineral average composition of individual thin section (Tables SI9 and SI10) and the total average composition calculated from the entire set of thin section. This result was expected due to the relative homogeneity of the chemical composition of the phenocrysts (Tables SI5–SI7).

[30] In this study, we considered that the surface of the thin section was representative of the analyzed samples. This hypothesis is opened to criticism, because the size of the rock chip could change from a sample to the other and because the structure of each rock sample could not be homogenous. To verify our approach, we compared the corrected whole rock major element composition of six samples to the average groundmass composition estimated from several SEM measurements realized across the thin sections. Because, the analyses from SEM are also quantitative, systematic bias exists between major chemical composition estimated by this method and geochemical analyses, as shown by the results obtained from the aphyric sample AF04. Consequently, the average chemical compositions of the groundmass estimated from SEM were calibrated using the aphyric sample AF04 as standard. The comparison between both approaches is presented in Figure SI45. Even if FeO and MgO contents of sample AF31 are slightly scattered, the data correlate with slopes close to ~1. Despite the uncertainties of both methods, these results show that our correction of whole-rock composition is correct.

6. Fractional Crystallization

[31] To discuss temporal variation in melt generation, we need to "see through" the effects of

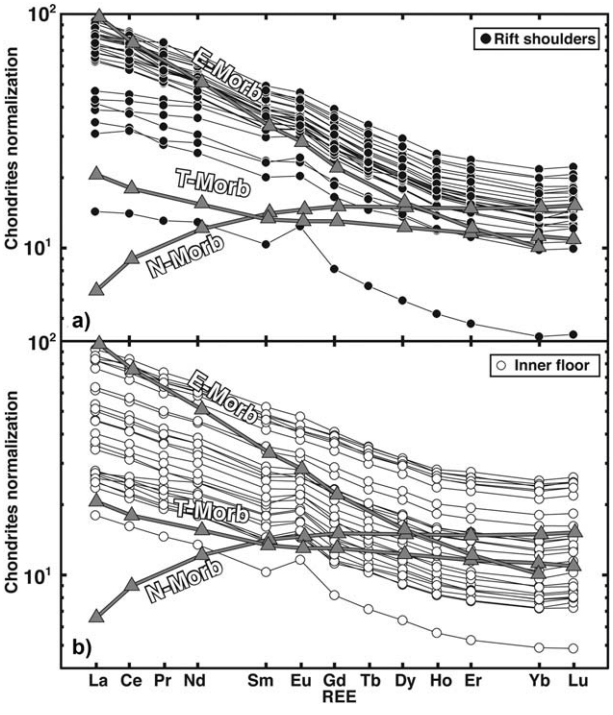

Figure 3. REE patterns for the (a) shoulders and (b) inner floor basalts of the Asal Rift. Normalization to chondritic values is from *Sun and McDonough* [1989]. Enriched E-MORB, Transitional T-MORB, and Normal N-MORB patterns are from *Langmuir et al*. [1992].

magmatic differentiation and to determine the geochemical characteristics of the parental magmas. Accordingly, the first problem is to identify the differentiation processes. Then, we can consider whether differentiation itself could have generated the separate geographical groups A and B in the Asal Rift or whether multiple parental magmas were actually required.

[32] Major elements variability across the rift (Figure 5) shows new tendencies that were not obvious using the uncorrected data set (Figure SI41). While SiO_2^* (SiO_2^* is SiO_2 corrected for phenocrysts accumulation, Tables SI9 and SI10) increases and FeO^*, TiO_2^* slightly decrease from the shoulders to the rift axis, MgO^*, $Al_2O_3^*$, CaO^*, Na_2O^*, and K_2O^* contents do not show clear trends across the rift. Samples also display better defined trends on MgO^* variation diagrams (Figure 6). The data show a rapid decrease in MgO^* accompanied by rapid increases in FeO^*, TiO_2^*, Na_2O^*, SiO_2^*, and decreases in CaO^* and $Al_2O_3^*$ consistent with gabbroic fractionation involving initial removal of olivine, followed by extraction of three-phase assemblage olivine-plagioclase-clinopyroxene.

[33] In order to test this hypothesis, we used the Liquid-Line of Descent (LLD) calculation procedure of *Weaver and Langmuir* [1990]. We have selected the most MgO^* rich sample as a parental magma composition (sample AF51) to quantitatively test the trends plotted in Figure 6. Fractional crystallization calculations were performed at 1 and 4 kbar with water content ranging from 1000 to 4000 ppm. The models satisfactorily explain the FeO^*, $Al_2O_3^*$, and CaO^* content of the lavas suite, suggesting that the data from the inner floor could derive from the crystallization at low pressure of magmas from the rift shoulders. However, SiO_2^*, TiO_2^*, Na_2O^*, and K_2O^* contents of the lava flows do not follow the computed LLDs. Different pressures of crystallization (1–4 kbar), or variable water content (1000–4000 ppm), are not appropriate to explain the whole data set from a single parental magma (i.e., sample AF51).

[34] Because high MgO^* lavas are missing from the inner floor Rift, we used melt inclusions trapped in Bytownite phenocrysts from the Ardoukoba eruption as a starting parental magma composition for the recent lava flows [*Clocchiatti and Massare*, 1985]. These high MgO liquid compositions (red dots in Figure 6) are different from those erupted on the rift shoulders (black dots with $MgO^* > 8\%$ in Figure 6). Fractional crystallization calculations were performed at 4 kbar with water content ranging from 1000 to 4000 ppm. The computed LLDs satisfactorily explain the most differentiated lavas from the inner floor (samples AF01–AF06 and AF63–AF64 for instance). We note however that for a given MgO^*, the modeled K_2O^* are shifted toward lower values. This apparent discrepancy has been previously noticed by *Clocchiatti and Massare* [1985]. It could be due to a systematic analytical bias on the measured K content of melt inclusions using electron microprobe.

[35] To summarize, in addition to the changes in melt composition produced during crystallization it is clear from the data reported in the Figure 6 that there is another aspect of the chemical variability. For example, the data at 7–9% MgO^* show variations in FeO^* contents ranging from 9% to 12%, Na_2O^* contents from 2% to 3%, and SiO_2^* contents from 47% to 49%. Because the samples are corrected for phenocryst accumulation, the difference in major element compositions at a given MgO^* content can only reflect changes in magma generation processes, such as variation of pressure and extent of melting, mantle source heterogeneities or contamination and assimilation effects.

In the following, we will detect, differentiate and constrain the contribution of these different processes.

7. Crustal Contamination and Source Heterogeneity

[36] In rift continental zones, contamination and assimilation processes could be a significant factor in the variations of the chemical composition. At the scale of the Afar Depression, previous works [*Deniel et al*., 1994; *Hart et al*., 1989] show that the younger differentiated lavas, from the Dalha series (<9 Ma) up to the youngest series (Asal Rift), do not isotopically differ from associated basalts, and were probably derived from them by fractional crystallization without significant crustal contamination. To assess the role of contamination at the scale of the Asal Rift, we used Sr and Nd isotopic ratios and major chemical composition corrected for phenocryst accumulation from previous studies [*Schilling et al*., 1992; *Deniel et al*., 1994; *Vigier et al*., 1999]. The data only cover the southern part of the rift (from ~530 kyr to the present). Because the filling of the Asal Rift is symmetrical (Figure 2) [*Manighetti et al*., 1998; *De Chabalier and Avouac*, 1994], we made the assumption that these samples are also representative of the northern part of the rift.

[37] If the crust contaminates the rising basaltic magmas, the more differentiated rocks should show the best evidence for contamination (higher degrees of differentiation imply longer periods of residence in the upper crustal magma chambers). Figure SI46A shows that $^{87}Sr/^{86}Sr$ basalt ratios are clustered around a mean value of 0.70354 ± 3 across the Asal Rift. These ratios are similar to those of the Asal rhyolitic domes, but lower than the Ali Adde rhyolite, which provides isotopic ratios of the local continental crust [*Deniel et al*, 1994; *Hegner and Pallister*, 1989]. In Figures SI46B and SI46C, the data suite also do not show any distinct trends between $^{87}Sr/^{86}Sr$ and fractionation indices (SiO_2 or Mg#). These results suggest that the differentiation of these magmas is not affected by assimilation-fractional crystallization process. The Nd-Sr isotopic diagram (Figure SI46D) also confirms the absence of the lithospheric component in the genesis of the Asal Rift basalt [*Deniel et al*., 1994]. The data form a cluster and overlap the field of MORB and Ocean Island Basalts. This mantle source affinity is also revealed from our data set and those of *Deniel et al*. [1994] from incompatible trace element ratios (Figure SI46E). A recent study [*Rooney et al*., 2012a] suggest that Hf-Pb data from the Asal Rift have affinity to, and overlap with, the East Sheba Ridge (Aden Ridge) data and has also Indian Ocean-like Hf and Pb isotope signatures [*Rooney et al*., 2012a]. However it has been also shown that these lava flows exhibit values consistent with mixing between Afar plume and regional lithospheric mantle [*Schilling et al*., 1992; *Rooney et al*., 2012a; *Rooney et al*., 2013]]. In the Afar depression, the isotopic signature of a mantle plume is most pronounced toward Djibouti [*Schilling et al*., 1992; *Rooney et al*., 2012a], consistent with maximum temperature values recorded in this area [*Rooney et al*., 2012b]. The lava flows from the Afar depression show that, with decreasing age, the isotopic properties of the basalts express a more depleted composition. This is interpreted simply as an increased contribution from the depleted upper mantle and a lessening of crustal assimilation [*Hart et al*., 1989]. A similar pattern is observed in Djibouti where early volcanic products (>10 Ma) exhibit substantial lithospheric contributions, but which become insignificant as rifting and lithospheric thinning progress, replaced by an increasing fraction of melt derived from depleted upper mantle and the Afar plume [*Deniel et al*., 1994]. Due to the small studied area, it is probable that the compositional heterogeneity beneath the Asal Rift is insignificant and thus do not impact the geneses of Basalts.

[38] Together, these results show that the major element variations at 7–9% MgO^*, which are observed in the binary diagrams (Figure 6), cannot be assigned to mantle source heterogeneities, contamination or assimilation effects. These important variations at a given MgO^* can be a consequence of pressure-release melting beneath the Asal Rift. To isolate the effects of mantle temperature, depth and extent of melting, it is first necessary to correct the variations caused by fractional crystallization.

8. Correction for Low Pressure Fractionation

[39] To correct the variations caused by fractional crystallization [*Klein and Langmuir*, 1987], FeO^* and Na_2O^* contents have been extrapolated along the LLD olivine-plagioclase-clinopyroxene slope to 8% MgO^*, using the algorithms of *Klein and*

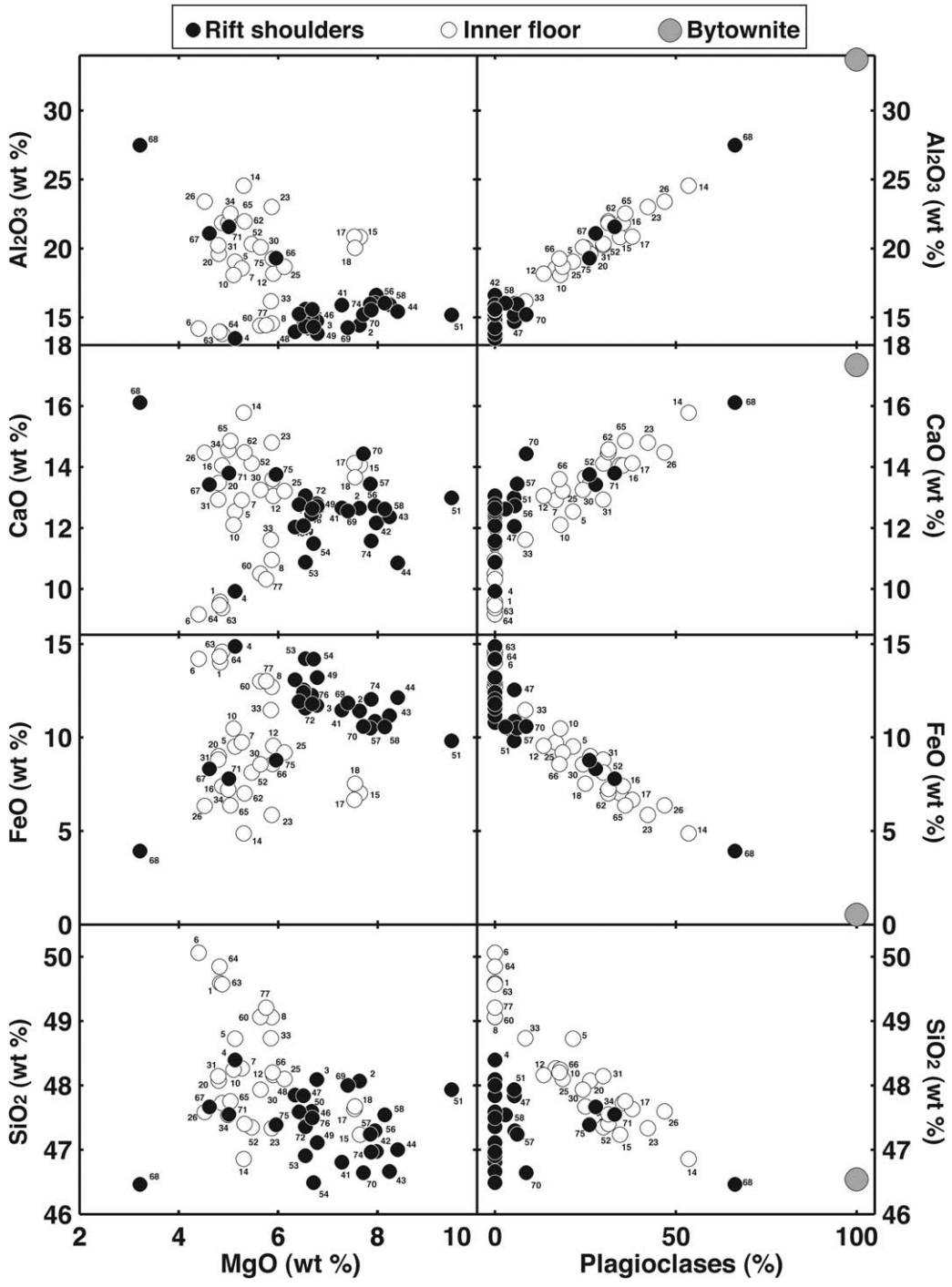

Figure 4. Illustration of the chemical variations due to the plagioclase. The relationship between the plagioclase abundance and Al_2O_3, CaO, FeO, and SiO_2 contents (noncorrected) is compared to the chemical composition plotted in binary diagrams. The linear relationship between the plagioclase abundance and major chemical composition of the samples show that the more the proportion of the plagioclase increases, the more the chemical composition of the samples is shifted toward the chemical composition of Bytownite. In the binary diagrams, the increase of Al_2O_3 and CaO and the decrease of FeO and SiO_2 contents are clearly explained as a dilution effect caused by addition of plagioclase accumulation.

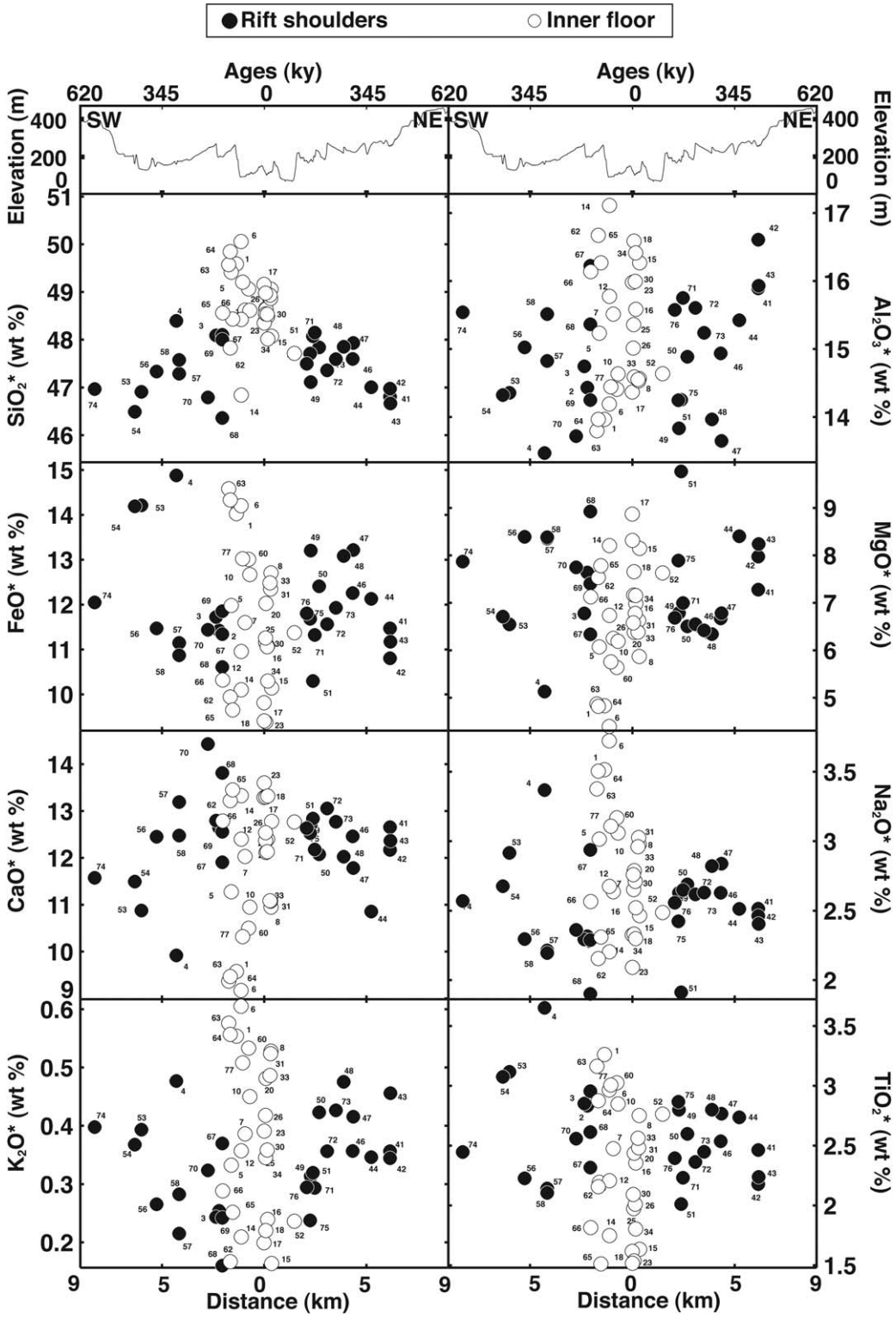

Figure 5. Major element composition of the samples corrected for mineral accumulation (*) across the Asal Rift.

Langmuir [1987], *Klein and Langmuir* [1989], and *Langmuir et al*. [1992] (Table SI11), whose slopes are equivalent to the LLD mean slopes in Figure 6.

[40] Samples from the rift shoulders (group B) are characterized by $Na_{8.0}^{*} = 2.29 \pm 0.06\%$, $Fe_{8.0}^{*} = 10.75 \pm 0.35\%$, $SiO_2^{*} = 47.70 \pm 0.27\%$,

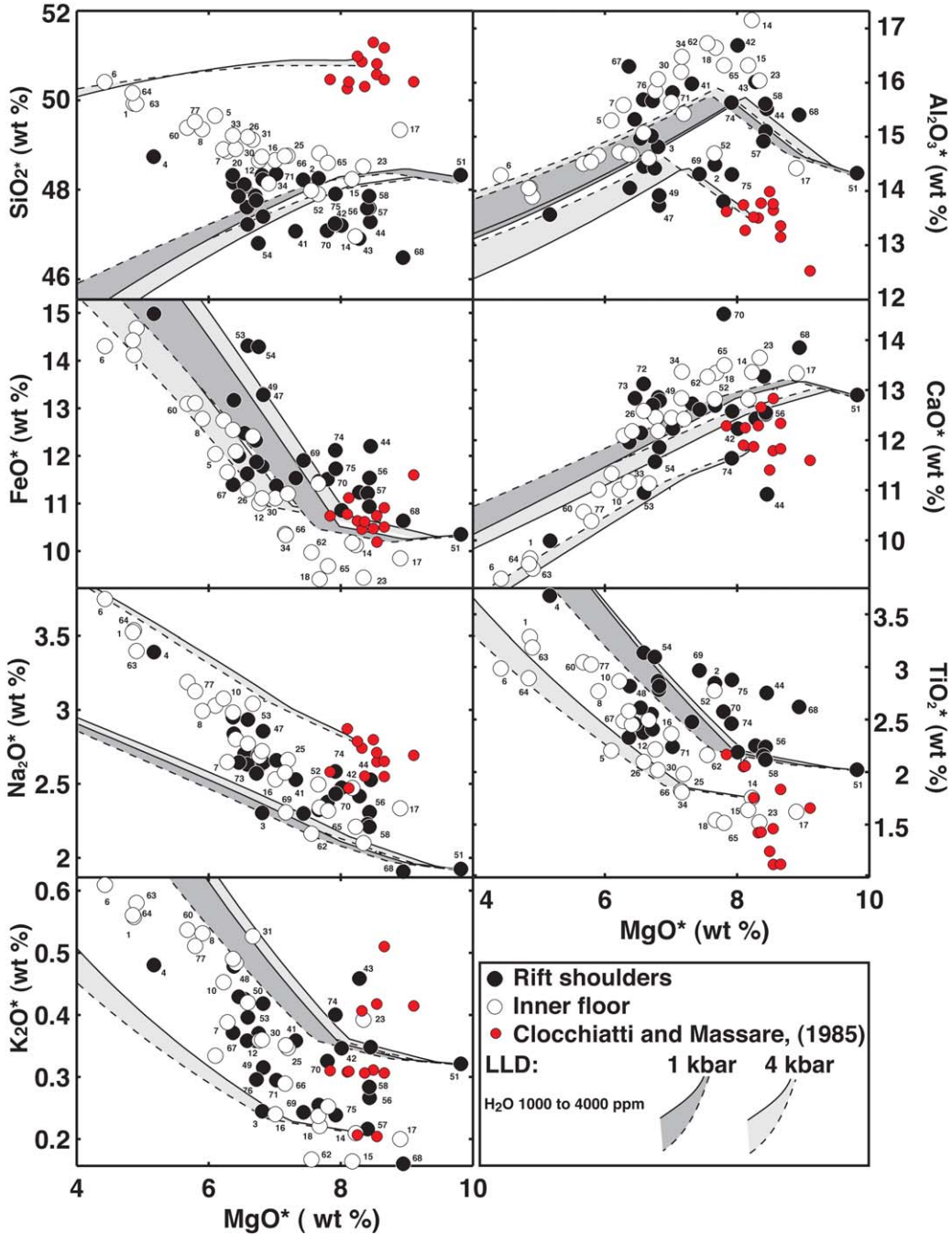

Figure 6. MgO variation diagrams for the samples of the Asal Rift corrected for mineral accumulation (asterisks). LLD are calculated using the procedure of *Weaver and Langmuir* [1990]. Fractional crystallization calculations were performed at 1 kbar and 4 kbar and water content ranging from 1000 (full line) to 4000 ppm (dashed line).

$Na^*/Ti^* = 2.54 \pm 0.12$ (large black dot in Figure SI47, Tables 1, SI9, and SI10 in supporting information). Samples from the inner floor (group A) are more homogeneous and characterized by lower $Fe_{8.0}{}^*$, higher $SiO_2{}^*$ and Na^*/Ti^* values ($9.41 \pm 0.21\%$, $48.95 \pm 0.35\%$ and 3.16 ± 0.20 respectively; large white dot in Figure SI47 in supporting information and Table 1). Equivalent values to those estimated from the whole data set can be obtained only using the aphyric samples (Table SI1 and SI2) of each group. For the inner floor samples (Group A), $Fe_{8.0}{}^* = 9.16 \pm 0.30\%$, $Na_{8.0}{}^* = 2.47 \pm 0.07\%$, $SiO_2{}^* = 49.81 \pm 0.30\%$, $Na^*/Ti^* = 2.86 \pm 0.17$, and for the

shoulder samples (Group B), $Fe_{8.0}^* = 10.73 \pm 0.45\%$, $Na_{8.0}^* = 2.31 \pm 0.08\%$, $SiO_2^* = 47.67 \pm 0.26\%$, $Na^*/Ti^* = 2.52 \pm 0.13$. This comparison suggests that our correction of whole-rock composition is correct. We also note that similar results can be calculated using the LLD calculation of *Danyushevsky and Plechov* [2011] or simple linear regressions trough the data (Figures SI48 and SI49).

[41] Figure 7 shows variations of $Fe_{8.0}^*$ and $Na_{8.0}^*$ across the Asal Rift. While $Na_{8.0}^*$ values do not show a clear trend across the rift ($Na_{8.0}^* = 2.35 \pm 0.06$), $Fe_{8.0}^*$ decreases from the rift shoulders to the rift axis. Since $Fe_{8.0}^*$ largely varies in proportion with initial pressure of melting, P_0 [e.g., *Langmuir et al.*, 1992, and references therein], the data suggest that the pressure of melting substantially decreases during the last 620 kyr beneath the Asal Rift.

[42] Thus, in the following section, we use a model to quantify the intensive parameters of the melting process (mantle temperature and pressure of melting) and test different mantle flow models (active flow and thick lithosphere).

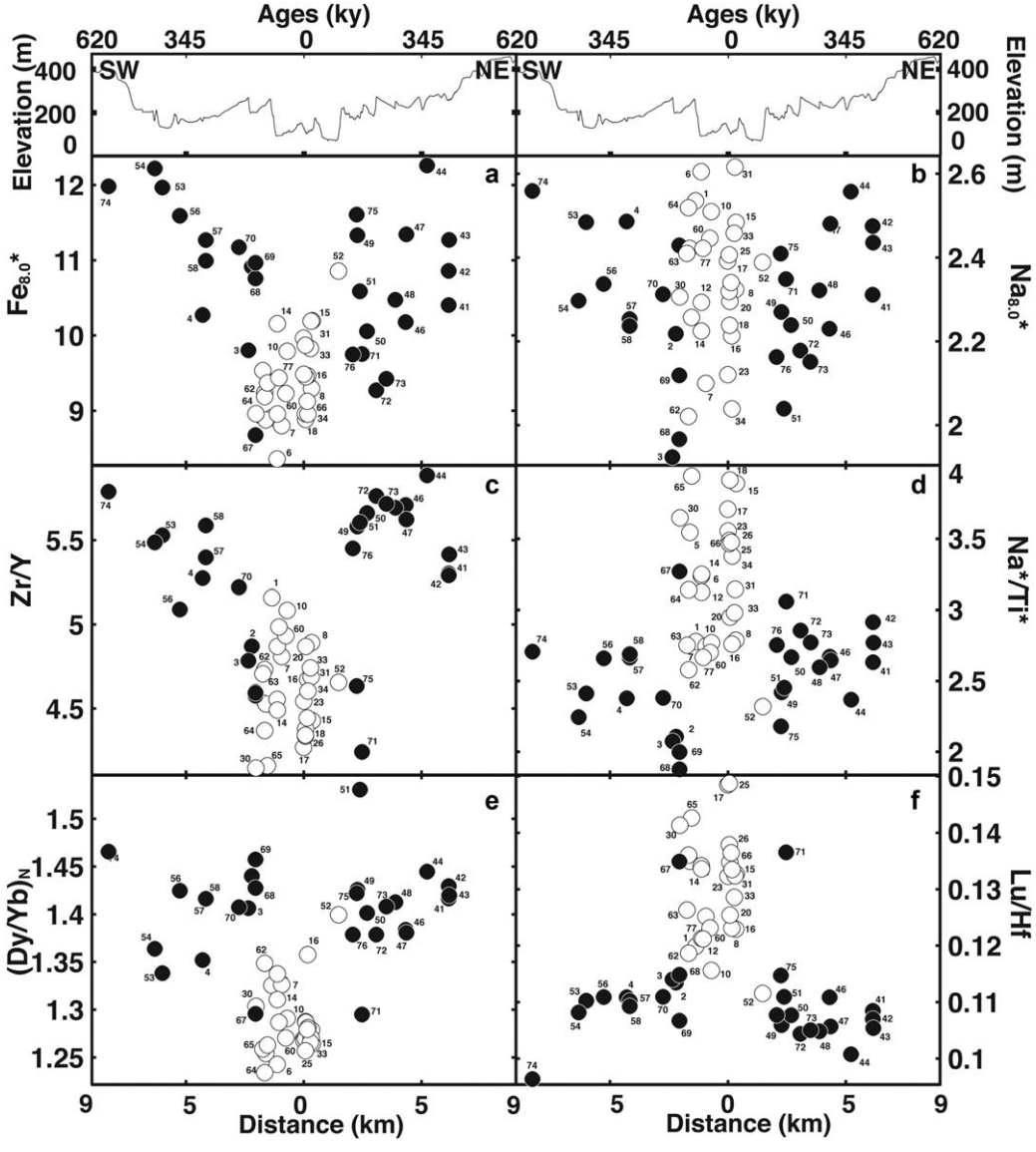

Figure 7. (a) $Fe_{8.0}^*$ decreases from the shoulders to the axis of the Asal Rift, suggesting a decrease of initial melting pressure and thus a decrease of the depths of melting, since 620 kyr. (b) $Na_{8.0}^*$ do not show a clear trend across the rift ($Na_{8.0} = 2.30 \pm 0.04\%$), suggesting that the extent of melting is rather constant since 620 kyr. (c–f) Variations of Zr/Y, Na^*/Ti^*, $(Dy/Yb)_N$, and Lu/Hf rations across the Asal. These variations are qualitatively consistent with shallow melting beneath the rift axis and deeper melting for off-axis lava flows.

9. Mantle Melting Models

[43] We use the model developed by *Langmuir et al*. [1992] to quantify the pressure and degree of mantle melting. This model describes compositional changes (MgO, FeO, Na_2O, SiO_2, TiO_2, and K_2O) in mantle melts during adiabatic decompression, assuming that olivine-melt equilibrium and trace element behavior for Na. The model is based on the partition coefficients (K_d) for Mg and Fe in olivine. The MgO and FeO concentrations in peridotite melts are imposed by olivine saturation and can be calculated from K_d expressions (which are themselves a function of P, T and alkali content). Na_2O is calculated from its K_d in clinopyroxene (which is also P and T dependent). Other inputs to the model include the initial composition of the mantle, the mantle solidus, and the relationship between T and F (% of melting) during isobaric and adiabatic melting.

[44] In our model, we use a normal peridotite composition with 15% clinopyroxene (MgO = 38.14 %, FeO = 8.30%, Na_2O = 0.26%, K_2O = 0.007%, and TiO_2 = 0.13%). After the mantle rises above its solidus, P_0 melt is extracted instantaneously from the residue up to the depth where upwelling and melting stop (P_f). Fractional melting paths generated by the model, which result in melt compositions between batch and fractional melts [*Langmuir et al*., 1992], are showed in Figure SI47 for Na_2O^* and FeO^* corrected to 8% MgO^* content (see supporting information). Each curve represents a different pressure of intersection with the mantle solidus P_0 from 20 to 45 kbar. P_0 will increase with increasing mantle potential temperature [*McKenzie and Bickle*, 1988]. As the mantle ascends above the solidus, the total melt fraction F increases until the pressure where the mantle ceases to ascend adiabatically (P_f) and therefore ceases to melt. The total melting column length P_0-P_f thus determines F. Increasing F has the main effect of lowering Na_2O in the melt, as Na_2O behaves as an incompatible element that is diluted by further increments of melting. FeO varies largely as a function of P_0, with relatively small variations as a function of F. The increase in FeO with increasing pressure is largely due to the effect of temperature on olivine K_d and the dominating effect of increasing temperature as pressure increases along the mantle solidus [*Langmuir et al*., 1992]. Thus the Na and Fe contents of mantle melts provide excellent constraints on the final depth of melting (from Na_2O which reflects F and therefore P_0-P_f) and on the initial depth of melting (from $Fe_{8.0}$).

[45] However, trace element patterns (Figure 5) and isotopic compositions [*Rooney et al*., 2012a; *Rooney et al*., 2013] show that the Asal Rift lava derived from a fertile source. Because the fertile mantle starts melting deeper and melts more, the calculated final pressures of melting slightly decrease, and the initial pressures and crust thicknesses slightly increase compared to a normal mantle composition. Using a fertile source with Na_2O = 0.28% and K_2O = 0.011%, the calculated crustal thickness beneath the Asal Rift is about 5 km (Table 2). This result is more consistent with the values estimated from geophysical measurement (Table 2), than the one estimated from a normal mantle composition (Na_2O = 0.26% and K_2O = 0.007%, Table 2). In the following, we will use a fertile mantle composition in the calculations.

9.1. Results of the Major Elements Forward Modeling

[46] The results of the inversions are presented in Table 1. The initial and final pressures of melting decrease regularly from the oldest to the most recent lava flows. The modeling results in Figure 8 show that the initial pressures of melting are ranging from 20 to 43 kbar and the final pressures of melting from 5 to 33 kbar. If the melting ceases when the upwelling mantle reaches the bottom of the lithosphere, the final pressure of melting can be converted to lithospheric thickness using the procedure of *Klein and Langmuir* [1987] and *Langmuir et al*. [1992]. Taking into account the average thicknesses estimated beneath the rift shoulders and the inner floor (Table 2), the lithospheric thickness decreases from 67 ± 8 to 43 ± 5 km in 620 kyr, corresponding to a lithospheric thinning rate of about 4.0 ± 2.0 cm yr^{-1}, which is consistent with the long-term spreading rate of the Asal Rift (2.9 ± 0.2 cm yr^{-1}, Figure SI39). As the average crustal thickness (4.95 ± 0.16 km), these lithospheric thicknesses are consistent with those estimated from geophysical measurement in the area (see section 2). Beneath the inner floor (group A, white arrows), melting paths are shallow (from 81 ± 4 to 43 ± 5 km) and are consistent with adiabatic melting in normal temperature asthenosphere (~1400°C), beneath an extensively thinned mantle lithosphere (Figure 8). On the contrary, melting on the rift shoulders (107 ± 7 to 67 ± 8 km) occurred beneath thicker lithosphere (group B, black arrows), requiring a mantle solidus temperature 100 ± 40°C hotter, which corresponds to a rate of mantle cooling of about 5×10^{-4} °C/yr.

Table 2. Average Temperatures, Pressures, and Thicknesses Estimated Beneath the Rift Shoulders (Group B) and the Inner Floor (Group A) for a Normal ($Na_2O = 0.26\%$, $K_2O = 0.007\%$) and Fertile ($Na_2O = 0.28\%$, $K_2O = 0.011\%$) Mantle Composition (See Text for More Details)[a]

Sample ID	Distance (m)	Mantle Compostion	Location	Age (kyr)	Temperature (°C)	P_o (kbar)	P_f (kbar)	F_{mean} (%)	D_c (km)	D_l (km)	D_m (km)
Inner Floor	785	Normal	A	54 ± 17	1466 ± 14	26.32 ± 1.18	14.33 ± 1.68	10.23	4.16 ± 0.41	44.48 ± 5.21	81.05 ± 3.67
Rift Shoulders	3893	Normal	B	268 ± 44	1566 ± 24	34.24 ± 2.00	22.26 ± 2.36	10.49	4.25 ± 0.36	69.00 ± 7.30	105.54 ± 6.15
Inner Floor	785	Fertile	A	54 ± 17	1471 ± 15	26.73 ± 1.21	13.70 ± 1.79	11.11	4.90 ± 0.51	42.70 ± 5.43	80.88 ± 4.48
Rift Shoulders	3893	Fertile	B	268 ± 44	1567 ± 25	34.75 ± 2.04	21.77 ± 2.49	11.35	5.00 ± 0.47	67.46 ± 7.57	106.75 ± 7.31
Geophysical observations									5	60–45	60–100

[a] P_0: initial pressure; P_f: final pressure; F_{mean} : mean extent of melting; D_c: thickness of the basaltic crust; D_l: thickness of the lithosphere; D_m: depth of the residual mantle base. Temperatures are solidus.

[47] We also note a good relationship between the SiO_2^* contents of lavas and their morphologies. While the massive and slightly fractured basaltic flows of the rift shoulders have low SiO_2^* contents, the viscous lava flows of the inner floor, which present more fissures and cracks, display higher SiO_2^* values. Equivalent values to those estimated from the whole data set are obtained only using the aphyric samples of each group. For the inner floor samples (Group A), $P_o = 25.60 \pm 1.91$ kbar, $P_f = 13.84 \pm 1.90$ kbar, $F_{mean}11.00 \pm 0.50\%$, $D_c = 4.19 \pm 0.37$ km, $D_l = 43.12 \pm 5.77$ km, $D_m = 78.65 \pm 5.87$ km, and for the shoulder samples (Group B), $P_o = 34.67 \pm 2.62$ kbar, $P_f = 21.80 \pm 3.30$ kbar, $F_{mean} = 11.00 \pm 0.50\%$, $D_c = 4.95 \pm 0.59$ km, $D_l = 67.45 \pm 10.12$ km, $D_m = 106.51 \pm 8.08$ km. Once more, this comparison shows that our correction of whole-rock composition is correct.

[48] At face value, FeO^* and SiO_2^* contents vary in inverse proportion across the Asal Rift (Figure 4). This variation is precisely expected for mantle melts derived from different melting depths, where higher pressure melts will have higher FeO but lower SiO_2 [*Niu and Batiza*, 1991; *Langmuir et al*., 1992; *Hirose and Kushiro*, 1993]. Using polynomial equation from *Wang et al*. [2002], which describes the relationship between SiO_2 concentration of peridotite melts and melting pressure from laboratory experiments [*Hirose and Kushiro*, 1993; *Robinson and Wood*, 1998; *Baker and Stolper*, 1994; *Walter*, 1998], we calculated melting pressure for the Asal Rift samples from the SiO_2^* contents. The comparison of melting pressures (P) calculated from SiO_2^* and from $Fe_{8.0}^*$ and $Na_{8.0}^*$ of Asal Rift basalts is presented in Figure SI50. Even if a low pressure offset exists between the two methods (underestimation of P based on Si due to the assumption of a single P of equilibration of polybaric melts, *Wang et al*. [2002]), the average melting pressures calculated from SiO_2^* content are reasonably well in agreement with the ranges calculated from $Fe_{8.0}^*$ end $Na_{8.0}^*$ (Table 1). As the SiO_2 method is independent and involves minimal treatment of the data or assumptions, this results gives supplementary support to the pressures sensitive calculated here. At last, we also note that the mean melting pressures (P) calculated from $Fe_{8.0}^*$ and $Na_{8.0}^*$ are similar to the predict pressures estimated from the thermobarometers for mafic magmas of *Lee et al*. [2009] (Figure SI51).

[49] In the following, we model sensitive pressure trace element partitioning in order to test the major element constraints on melting history in this area.

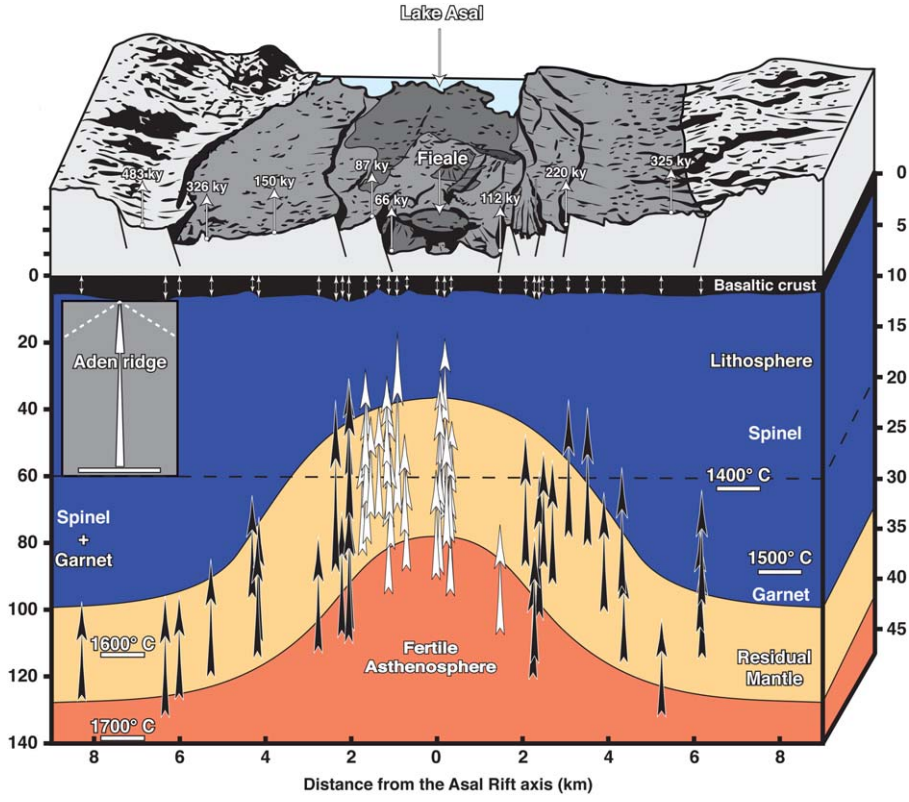

Figure 8. Melting regime across the Asal Rift. The small double white arrows illustrate the crustal thickness beneath the Asal Rift (4.95 ± 0.16 km). The large black and white arrows represent the melting columns calculated from each samples, based on the $Fe_{8.0}$ and $Na_{8.0}$ values (Table 1). The bottom of the arrow marks the onset of melting at the solidus and is a function of mantle temperature. The depths of melting were calculated from the procedure of *Klein and Langmuir* [1987] and *Langmuir et al*. [1992]. The model outputs show that beneath the rift axis, melting paths are shallow, from 81 ± 4 to 43 ± 5 km. These melting paths are consistent with adiabatic melting in normal temperature fertile asthenosphere (about 1400°C), beneath an extensively thinned mantle lithosphere. On the contrary, melting on the rift shoulders (107 .7 to 67.8 km) occurred beneath a thick mantle lithosphere and required mantle solidus temperature 100 ± 40°C hotter. The calculated rate of lithospheric thinning is 4.0 ± 2.0 cm yr^{-1}. The height of the Aden Ridge melting column is calculated from the samples of *Cann* [1970] and *O'Reilly et al*., [1993].

10. Constraints From the REE and HFSE on Melting Depth

[50] In basalts, REE, High Field Strength Elements (HFSE), Na and Ti are commonly used to constrain the mantle melting depths [*Fram et al*., 1998; *Putirka*, 1999; *Wang et al*., 2002]. Heavy REE and HFSE favor garnet structure, because their partition coefficients change during melting of spinel versus garnet peridotites. For a given melting column, melts in equilibrium with garnet will produce high Zr/Y, $(Dy/Yb)_N$ ratios and low Lu/Hf. These ratios will be gradually reversed as the melting column enters in the spinel filed. Because the K_{Na} of cpx/melt increases with increased *P*, while clinopyroxene and garnet K_{Ti} min/melt remain constant or decrease, Na/Ti ranges in the same way as Lu/Hf ratio [*Putirka*, 1999]. Figure 7 shows the variations of Zr/Y, $(Dy/Yb)_N$, Lu/Hf, and Na^*/Ti^* ratios across Asal Rift. While Zr/Y and $(Dy/Yb)_N$ increase with $Fe_{8.0}{}^*$ from the rift axis toward the rift shoulders, Lu/Hf and Na^*/Ti^* ratio decrease, which is consistent with the depth variations of pressure of melting. To test this hypothesis more quantitatively, we use the pressures of melting (P_0 and P_f) calculated from $Fe_{8.0}{}^*$ and $Na_{8.0}{}^*$ contents to predict what Lu/Hf ratio of the basalt should be.

[51] Our procedure is based on *Fram et al*. [1998] and *Wang et al*. [2002]. We observe that in Asal basalts, $Fe_{8.0}{}^*$ scales linearly with both P_0 and P_f (see Table 1). The relationships between $Fe_{8.0}{}^*$

and P_0, and between $Fe_{8.0}^*$ and P_f are expected because $Na_{8.0}^*$ are fairly constant across the rift and thus the interval P_0–P_f is also constant (13 ± 0.5 kbar). We used these linear relationships to calculate Lu/Hf fractionation in the basalts. As for the major element model, we compute polybaric melting along an adiabat in a single mantle melting column, using P_0 and P_f as calculated from FeO^* and Na_2O^*, and a linear melt productivity of 1.2% per kilobar of pressure decrease above the solidus. We start with a mantle mineral mode consistent with a fertile lherzolite (ol: 0.55; opx: 0.25; cpx: 0.15; gt: 0.05). The primitive mantle starting composition and chondrite normalization for Lu and Hf are from *Sun and McDonough* [1989], and partitioning coefficient mineral are from *Gibson and Geist* [2010] and *McKenzie and O'Nions* [1991] (Table SI12).

[52] Based on *Robinson and Wood* [1998], *Kinzler and Grove* [1992], *Falloon and Green* [1988], and *Takahashi and Kushiro* [1983], we consider that garnet to spinel transition occurs between 30 and 20 kbar (Table SI13). These ranges of pressure are coherent with the experimental data realized by *Klemme* [2004] and *Klemme and O'Neill* [2000]. In between each increment of melting, the mantle composition is revised to take into account depletion due to melting and pressure dependent phase transitions. Mantle composition is monitored by modal proportions of phases (Table SI14). The transitions from garnet to spinel occur over intervals rather than at discrete pressures. This approximates the natural situation where the phase transitions are gradual due to solid solution in all of the phases [*Fram et al*., 1998].

[53] Results of the melting model are show in Figure 9. The curve is constrained by the data, reproducing high Lu/Hf at low $Fe_{8.0}^*$ and low Lu/Hf at high $Fe_{8.0}^*$. For high $Fe_{8.0}^*$ values, Lu is held in the garnet, so Lu/Hf remains low. As melting continues, $Fe_{8.0}^*$ decreases, and garnet is exhausted or melting crosses into the spinel field, Lu is no longer retained in the residue, and Lu/Hf ratios rise. The data are well fit by the curve, which shows that the older lava flows were respectively generated in the garnet field, and the majority of the recent lava flows were produced in the garnet-spinel transition zone. The model reproduces the range of the Lu/Hf ratio and also validates the melting pressures calculated from major element melting model.

11. Conclusions and Discussions

[54] Because it has been shown in the literature that the recent basalts (<1 Ma) from the Asal Rift

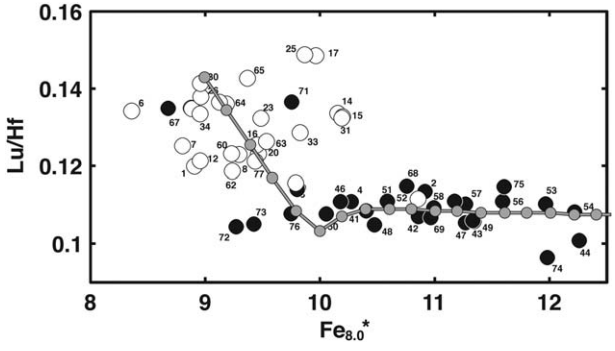

Figure 9. (a) Lu/Hf versus $Fe_{8.0}$ for or calculated mantle melts illustrating the effects of mantle composition, and melting systematics on melt compositions. The data are well fit by the curve, which shows that the majority of older lava and the most recent lava were, respectively, generated in the garnet and spinel field. The model reproduces the range of the Lu/Hf ratio and also validates the melting pressures calculated from element melting model.

cannot be assigned to mantle source heterogeneities, contamination or assimilation effects [*Hart et al*., 1989; *Barrat et al*., 1990; *Schilling et al*., 1992; *Deniel et al*., 1994; *Vigier et al*., 1999; *Rooney et al*., 2012], the chemical composition of quaternary lavas can be confidently used to constrain the temporal evolution of the rifting processes over the last 620 kyr.

(1) The major element composition of these lavas shows significant variations. These inferred differences in basalt chemistry are due principally to variable proportions of minerals in the whole-rocks, which leads to uncertainty in the interpretation of the major and trace elements. In the porphyric samples (that is ~54% of the data set), the mineral assemblages can be divided into two groups according to their morphology and chemical composition. Megacrysts of plagioclase (An_{76-88}), olivine (Fo_{60-80}) and clinopyroxene (Di_{40-42} En_{26-30} Fs_{6-9}) can be easily identified by their important size (up to ~1 cm) and their characteristic resorption figures (rounded shapes, corrosion embayments). The groudmass is characterized by equilibrium textures, euhedral phenocrysts of smaller size and more evolved compositions than those of the first group. The olivine composition ranges from Fo_{53} to Fo_{66}, the plagioclase laths lie between An_{60} and An_{72} and clinopyroxene microlites are Di_{32-38} En_{18-26} Fs_{8-12}.
(2) In order to correct the whole rock chemistry for megacrysts accumulation, we used a simple mass balance calculation. The corrected

compositions correlate with the mean groundmass compositions determined using Scanning Electron Microscopy. The major elements corrected for mineral accumulation and the aphyric samples do not define a single trend in binary diagrams. The difference in major element at a given MgO^* content can only reflect changes in melting processes. Trace element ratios (Lu/Hf, Zr/Y, and Dy/Yb_N) and major element compositions corrected for mineral accumulation and crystallization ($Na_{8.0}^*$, $Fe_{8.0}^*$, SiO_2^*, and Na^*/Ti^*) show a symmetric pattern relative to the rift axis.

(3) The results obtained from the major element inversion are coherent with seismic refraction and seismological data. For a fertile mantle composition ($Na_2O = 0.28\%$, $K_2O = 0.011\%$), upwelling model combined with variable initial and final pressures of melting explain the observed $Na_{8.0}^* - Fe_{8.0}^*$ values. The final pressures of melting (P_f) are thus interpreted as a "petrologically constrained lithospheric thickness" where mantle melting stopped.

(4) The resulting model outputs show that beneath the rift axis, melting paths are shallow, from 81 ± 4 to 43 ± 5 km. These melting paths are consistent with adiabatic melting in normal-temperature fertile asthenosphere, beneath an extensively thinned mantle lithosphere. On the contrary, melting on the rift shoulders occurred beneath a thick mantle lithosphere and required mantle solidus temperature $100 \pm 40°$ C hotter (melting paths from 107 ± 7 to 67 ± 8 km), which corresponds to a rate of mantle cooling of about 5×10^{-4} °C/yr. Our data strengthen the recent results of *Rooney et al*. [2012b], which show that elevated mantle temperatures are pervasive feature of the upper mantle beneath the East Africa. They noted a maximum temperature anomaly of 140°C above ambient mantle recorded from magmas youngers than 10 Myr erupted in Djibouti.

(5) The modeled Lu/Hf ratios coincide with the observed ratios suggesting that the major element melting model is correct and that garnet is required to explain the rift shoulders basalts chemistry. Finally, the calculated rate of lithospheric thinning estimated from these results is about 4.0 ± 2.0 cm yr^{-1}, which is consistent with the long-term spreading rate of the Asal Rift.

Acknowledgments

[55] We thank Pays de la Loire Region (France) for funding this project. We are grateful to the Arta Observatory Staff and to the CERD researchers for their constant scientific help and collaboration. We thank Cecile Doubre who greatly participated to the data acquisition in the Asal Rift, Antoine Bézos for fruitful discussions and for provide us a modified version of the Liquid-Line of Descent calculation procedure of *Weaver and Langmuir* [1990], and Patrick Launeau for provide us the image2003 software. We also thank the French Army in Djibouti, which allowed us to work in the best conditions. Tyrone Rooney and an anonymous reviewer provided detailed and helpful reviews, which enhanced the manuscript. Finally, we thank Cin-Ty Lee for careful editorial handling.

References

Baker, M. B., and E. M. Stolper (1994), Determining the composition of high-pressure mantle melts using diamond aggregates, *Geochim. Cosmochim. Acta*, *58*, 2811–2827.

Barrat, J. A., B. M. Jahn, J. L. Joron, B. Auvray, and H. Hamdi (1990), Mantle heterogeneity in northeastern Africa: Evidence from Nd isotopic compositions and hygromagmaphile element geochemistry of basaltic rocks from the Gulf of Tadjoura and Southern Red Sea regions, *Earth Planet. Sci. Lett.*, *101*, 233–247.

Bastow, I. D., and D. Keir (2011), The protracted development of the continent–ocean transition in Afar, *Nat. Geosci.*, *4*(4), 248–250.

Berckhemer, H., B. Baier, H. Bartelsen, A. Behle, H. Burckhardt, H. Gebrande, J. Makris, H. Menzel, H. Miller, and R. Vees (1975), *Deep seismic soundings in the Afar region and on the highland of Ethiopia, in Afar Depression of Ethiopia*, edited by A. Pilger and A. Rosler, pp. 89–107, Schweizerbart, Stuttgart, Germany.

Bizouard, H., J.-B. Clocchiatti, R. Ruegg, and G. Marinelli (1980), Les tholéiites à olivine à mégacristaux de bytownite du rift d'Asal (République de Djibouti), Quelques suggestions pour un modèle génétique, *Bull. Soc. Geol. Fr.*, *22*(6), 845–850.

Bradshaw, T. K., C. Hawkesworth, and K. Gallagher (1993), Basaltic volcanism in the Southern Basin and Range: No role for a mantle plume, *Earth Planet. Sci. Lett.*, *116*, 45–62.

Cann, J. R. (1970), Petrology of basalts dredged from the Gulf of Aden, *Deep Sea Res.*, *17*, 477–482.

Cloetingh, C., and R. Wortel (1986), Stress in the Indo-Australian plate, *Tectonophysics*, *132*, 49–67, doi:10.1016/0040-1951(86)90024-7.

Clocchiatti, R., A. Havette, J. Weiss, and S. Wilhelm (1978), Les Bytownites du Rift d'Asal, Premiere partie, Etude des verres basaltiques inclus dans les mégacristaux: Nouvelle approche pour la connaissance de certains processus pétrogénétiques, *Bull. Soc. Fr. Miner. Crystallogr.*, *101*, 66–76.

Clocchiatti, R., and D. Massare (1985), Experimental crystal growth in glass inclusions: The possibilities and limits of the method, *Contrib. Mineral. Petrol.*, *89*(2-3), 193–204, doi:10.1007/BF00379453.

Courtillot, V. E. (1980), Opening of the Gulf of Aden and Afar by progressive tearing, *Phys. Earth Planet. Inter.*, *21*, 343–350, doi:10.1016/0031-9201(80)90137-5.

Courtillot, V., C. Jaupart, I. Manighetti, P. Tapponnier, and J. Besse (1999), On causal links between flood basalts and continental breakup, *Earth Planet. Sci. Lett.*, *166*(3-4), 177–195, doi:10.1016/S0012-821X(98)00282-9.

Danyushevsky L. V. and Plechov P. (2011), Petrolog3: Integrated software for modeling crystallization processes., *Geochemistry Geophysics Geosystems*, *12*: doi: 10.1029/2011GC003516. issn: 1525–2027.

De Chabalier, J.-B., and J.-P. Avouac (1994), Kinematics of the Asal Rift (Djibouti) determined from the deformation of Fieale Volcano, *Science*, *265*, 1677–1681.

Demange, J., and Puvilland P., Le champ géothermique d'Asal, Djibouti, synthése des données (Compagnie frañaise pour le d'veloppement de la géothermie, report 33CFG06, Orleans).

Deniel, C., P. Vidal, C. Coulon, P.-J. Vellutini, and P. Piguet (1994), Temporal evolution of mantle sources during continental rifting: The volcanism of Djibouti (Afar), *J. Geophys. Res.*, *99*, 2853–2869.

DePaolo, D. J., and E. E., Daley (2000), Neodymium isotopes in basalts of the southwest basin and range and lithospheric thinning during continental extension, *Chem. Geol.*, *169*(1-2), 157–185.

Doubre, C., I. Manighetti, C. Dorbath, L. Dorbath, E. Jacques, and J. C. Delmond (2007a), Crustal structure and magmatotectonic processes in an active rift (Asal-Ghoubbet,Afar, East Africa): 1. Insights from a 5-month seismological experiment, *J. Geophys. Res.*, *112*, B05405, doi:10.1029/2005JB003940.

Doubre, C., I. Manighetti, L. Dorbath, C. Dorbath, D. Bertil, and J. C. Delmond (2007b), Crustal structure and magmatotectonic processes in an active rift (Asal-Ghoubbet, Afar, East Africa): 2. Insights from the 23-year recording of seismicity since the last rifting event, *J. Geophys. Res.*, *112*, B05406, doi:10.1029/2006JB004333.

Dunbar, J. A., Sawyer D. S., (1989), How preexisting weaknesses control the style ofcontinental breakup, *J. Geophys. Res.*, *94*, 7278–7292.

Dungan, M. A., M. M. Lindstrom, N. J. MacMillan, S. Moorbath, J. Hoefs, and L. A. Haskin (1986), Open system magmatic evolution of the Taos Plateau volcanic field, northern New Mexico: 1. The petrology and geochemistry of the Servilleta basalt, *J. Geophys. Res.*, *91*, 5999–6028.

Ebinger, C. J., D. Keir, A. Ayele, E. Calais, J. T. Wright, M. Belachew, S. O. J. Hammond, E. Campbell, and R. W. Buck (2008), Capturing magma intrusion and faulting processes during continental rupture: Seismicity of the Dabbahu (Afar) rift, *Geophys. J. Int.*, *174*(3), 1138–1152.

Falloon, T. J., and H. D. Green (1988), Anhydrous partial melting of peridotite from 8 to 35 kb and the petrogenesis of MORB, *J. Petrol.*, 379–414. (Special Lithosphere Issue).

Ferguson, D. J., A. T. Calvert, D. M. Pyle, D. J. Blundy, G. Yirgu, and J. T. Wright (2013), Constraining timescales of focused magmatic accretion and extension in the Afar crust using lava geochronology, *Nat. Commun.*, *4*, 1416, doi:10.1038/ncomms2410.

Fram, M. S., C. E. Lesher, and A. M. Volpe (1998), Mantle melting systematics: Transition from continental to oceanic volcanism on the southeast Greenland margin, *Proc. Ocean Drill. Program Sci. Results*, *152*, 373–386.

Glazner, A. F., G. L. Farmer, W. T. Hughes, J. L. Wooden, and W. Pickthorn (1991), Contamination of basaltic magma by mafic crust at Amboy and Pisgah Craters, Mojave Desert, California, *J. Geophys. Res.*, *96*, 13,673–13,691.

Gibson, S. A., and D. Geist (2010), Geochemical and geophysical estimates of lithospheric thickness variation beneath Galápagos, *Earth Planet. Sci. Lett.*, *300*, 275–286.

Glazner, A. F., and G. L. Farmer (1992), Production of isotopic variability in continental basalts by cryptic crustal contamination, *Science*, *255*, 72–74.

Hammond, J. O. S., J.-M. Kendall, G. W. Stuart, D. Keir, C. J. Ebinger, A. Ayele, and M. Belachew (2011), The nature of the crust beneath the Afar triple junction: Evidence from receiver functions, *Geochem. Geophys. Geosyst.*, *12*, Q12004, doi:10.1029/2011GC003738.

Hart, W. K., G. Woldegabriel, C. R. Walter, and A. S. Mertzman (1989), Basaltic volcanism in Ethiopia: Constraints on continental rifting and mantle interactions, *J. Geophys. Res.*, *94*, 7731–7748.

Hayward, N. J., and C. J. Ebinger (1996), Variations in the along-axis segmentation of the Afar Rift system, *Tectonics*, *15*, 244–256, doi:10.1029/95TC02292, ISSN: 0278–7407.

Hegner, E., and J. Pallister (1989), Pb, Sr, and Nd isotopic characteristics of Tertiary Red Sea rift volcanics from the central Saudi Arabian coastal plain, *J. Geophys. Res.*, *94*, 7749–7755.

Hirose, K., and I. Kushiro (1993), artial melting of dry peridotites at high pressures: Determination of compositions of melts segregated from peridotite using aggregates of diamond, *Earth. Planet. Sci. Lett.*, *114*, 477–489, doi:10.1016/0012-821X(93)90077-M.

Hofmann, C., V. Courtillot, G. Féraud, P. Rochette, G. Yirgu, E. Ketefo, and R. Pik (1997), Timing of the Ethiopian flood basalt event and implications for plume birth and global change, *Nature*, *389*, 838–841, doi:10.1038/39853.

Kempton, P. D., J. G. Fitton, C. J. Hawkesworth, and D. S. Ormerod (1991), Isotopic and trace element constraints on the composition and evolution of the lithosphere beneath the southwestern United States, *J. Geophys. Res.*, *96*, 13,713–13,735.

Kinzler, R. J., and L. T. Grove (1992), Primary magmas of mid-ocean ridge basalts: 1. Experiments and methods, *J. Geophys. Res.*, *97*, 6885–6906.

Klein, E. M., and C. H. Langmuir (1987), Global correlations of ocean ridge basalt chemistry with axial depth and crustal thickness, *J. Geophys. Res.*, *92*, 8089–8115.

Klein, E., and C. Langmuir (1989), Local versus global variations in ocean ridge basalt composition: A reply, *J. Geophys. Res.*, *94*, 4241–4252.

Klemme, S. (2004), The influence of Cr on the garnet-spinel transition in the Earth's mantle: Experiments in the system MgO-Cr2O3-SiO2 and thermodynamic modeling, *Lithos*, *77*, 639–646.

Klemme, S., and H. S. O'Neill (2000), The near-solidus transition from garnet lherzolite to spinel lherzolite, *Contrib. Mineral. Petrol.*, *138*, 237–248.

Knox, R. P., A. A. Nyblade, and C. A. Langston (1998), Upper mantle S velocities beneath Afar and western Saudi Arabia from Rayleigh wave dispersion, *Geophys. Res. Lett.*, *25*, 4233–4236, doi:10.1029/1998GL900130.

Lahitte, P., P.-Y. Gillot, T. Kidane, V. Courtillot, and A. Bekele (2003), New age constraints on the timing of volcanism in central Afar, in the presence of propagating rifts, *J. Geophys. Res.*, *108*(B2), 2123, doi:10.1029/2001JB001689.

Langmuir, C. H., E. M. Klein, and T. Plank (1992), *Petrological Systematics of Mid-Ocean Ridge Basalts: Constraints on Melt Generation Beneath Ocean Ridges, Geophys. Monogr. Ser.*, vol. *71*, pp. 183–280, AGU, Washington, D. C.

Launeau, P., and P.-Y. F. Robin (1996), Fabric analysis using the intercept method, *Tectonophysics*, *267*(1-4), 91–119.

Lee, C.-T. A., P. Luffi, T. Plank, H. A. Dalton, and W. P. Leeman (2009), Constraints on the depths and temperatures of basaltic magma generation on Earth and other terrestrial planets, *Earth Planet. Sci. Lett.*, *279*, 20–33.

Lépine, J.-C., and A. Hirn (1992), Seismotectonics in the Republic Of Djibouti, linking the Afar depression and the Gulf of Aden, *Tectonophysics*, *209*, 65–86.

Lin, J., and Parmentier E, M. (1990), A finite amplitude necking model of rifting in brittle lithosphere., *J. Geophys. Res*, *95*, 4909–4924.

Makris, J., and A. Ginzberg (1987), The Afar depression: Transition between continental rifting and sea-floor spreading, in *Sedimentary Basins Within the Dead Sea and Other Rift Zones*, edited by Z. Ben Avrahem, *Tectonophysics*, *141*, 199–214.

Manighetti, I., P. Tapponnier, P. Y. Gillot, E. Jacques, V. Courtillot, R. Armijo, J. C. Ruegg, and G. King (1998), Propagation of rifting along the Arabia-Somalia plate boundary: Into Afar, *J. Geophys. Res.*, *103*, 4947–4974, doi:10.1029/97JB02758.

Manighetti, I., P. Tapponnier, V. Courtillot, Y. Gallet, E. Jacques, and P.-Y. Gillot (2001), Strain transfer between disconnected, propagating rifts in Afar, *J. Geophys. Res.*, *106*, 13,613–13,665.

Marty, B., I. Appora, J. A. Barrat, C. Deniel, P. Vellutini, and P. Vidal (1993), He, Ar, Sr, Nd and Pb isotopes in volcanic rocks from Afar: Evidence for a primitive mantle component and constraints on magmatic sources, *Geochem. J.*, *27*, 219–228.

McKenzie, D., and M. J. Bickle (1988), The volume and composition of melt generated by extension of the lithosphere, *J. Petrol.*, *29*, 625–679.

McKenzie, D., and R. K. O'Nions (1991), Partial melt distributions from inversion of rare Earth element concentrations, *J. Petrol.*, *32*, 1021–1091.

Niu, Y. L., and R. Batiza (1991), An empirical method for calculating melt compositions produced beneath mid-ocean ridges: Application for axis and off-axis (seamounts) melting, *J. Geophys. Res.*, *96*, 21,753–21,777.

Nyblade, A. A., R. P. Knox, and H. Gurrola (2000), Mantle transition zone thickness beneath Afar: Implications for the origin of the Afar hotspot, *Geophys. J. Int.*, *142*, 615–619.

O'Reilly, W., K. Brown, P. Styles, and T. W. Bloxam (1993), A detailed geochemical and rock magnetic study of dredged basalt from th Sheba Ridge, *Gulf of Aden, Mar. Geophys. Res.*, *15*, 101–119.

Parsons, T., G. A. Thompson, and N. H. Sleep (1994), Mantle plume influences on the Neogene uplift and extension of the U.S. western cordillera?, *Geology*, *22*, 83–86.

Petruk, W. (1989), *Image analysis of minerals, in Short Course on Image Analysis Applied to Mineral and Earth Sciences*, edited by W. Petruck, pp. 6–18, Mineral. Assoc. of Can., Ottawa.

Pinzuti, P., A. Mignan, and G. C. P. King (2010), Surface morphology of active normal faults in hard rock: Implications for the mechanics of the Asal Rift, Djibouti, *Earth Planet. Sci. Lett.*, *299*(1-2), 169–179.

Putirka, K. (1999), Melting depths and mantle heterogeneity beneath Hawaii and the East Pacific Rise: Constraints from Na/Ti and REE ratios, *J. Geophys. Res.*, *104*, 2817–2829.

Richard, O. (1979), Etude de la transition dorsale océanique-rift émergé: Le golfe de Tadjoura, PhD thesis, Univ. d'Orsay, Paris.

Robinson, J. A. C., and B. J. Wood (1998), The depth of the spinel to garnet transition at the peridotite solidus, *Earth. Planet. Sci. Lett.*, *164*, 277–284, doi:10.1016/S0012-821X(98)00213-1.

Rooney, T., T. Furman, I. Bastow, D. Ayalew, and G. Yirgu (2007), Lithospheric modification during crustal extension in the Main Ethiopian Rift, *J. Geophys. Res.*, *112*, B10201, doi:10.1029/2006JB004916.

Rooney, T. O., B. B. Hanan, D. W. Graham, T. H. Furman, J. Blichert-Toft, and J. G. Schilling (2012a), Upper mantle pollution during Afar plume-continental rift interaction, *J. Petrol.*, *53*, 365–389.

Rooney, T. O., C. Herzberg, and I. D. Bastow (2012b), Elevated mantle temperature beneath East Africa, *Geology*, *40*, 27–30, doi:10.1130/G32382.1.

Rooney, T. O., P. Mohr, L. Dosso, and C. Hall (2013), Geochemical evidence of mantle reservoir evolution during progressive rifting along the western Afar margin, *Geochim. Cosmochim. Acta*, *101*, 65–88.

Ruegg, J.-C. (1975), Structure profonde de la croûte et du manteau supérieur du Sud-Est de l'Afar d'après les données sismiques, *Ann. Geophys.*, *31*, 329–360.

Ruegg, J.-C., and M. Kasser. (1987), Deformation across the Asal-Ghoubbet Rift, Djibouti, uplift and crustal extension, 1979–1986, *Geophys. Res. Lett.*, *14*, 745–748.

Rychert, C. A., J. O. S. Hammond, N. Harmon, J.-M. Kendall, D. Keir, C. Ebinger, I. D. Bastow, A. Ayele, M. Belachew, and G. Stuart (2012), Volcanism in the Afar Rift sustained by decompression melting with minimal plume influence, *Nat. Geosci.*, *5*, 406–409.

Schilling, J.-G. (1973), Iceland mantle plume, *Nature*, *246*, 141–143, doi:10.1038/246141a0.

Schilling, J.-G., R. H. Kingsley, B. B. Hanan, and B. L. McCully (1992), Nd-Sr-Pb isotopic variations along the Gulf of Aden - Evidence for Afar mantle plume-continental lithosphere interaction, *J. Geophys. Res.*, *97*, 10,927–10,966.

Stieltjes , L. (1980), Geological Map of Asal Rift, Republic of Djibouti, scale 1/50000, Centre National de la Recherche Scientifique, Paris.

Sun, H. S., and W. F. McDonough (1989), Chemical and isotopic systematics of oceanic basalts: Implications for mantle composition and processes, in *Magmatism in the Ocean Basins*, edited by A. D. Saunders and M. J. Norry, Geol. Soc. Spec. Publ., *42*, 313–345.

Takahashi, E., and I. Kushiro (1983), Melting of a dry peridotite at high pressures and basalt magma genesis, *Am. Mineral.*, *68*, 859–879.

Tarantola, A., J. C. Ruegg, and J. P. Lepine (1980), Geodetic evidence for rifting in afar, 2. Vertical displacements, *Earth Planet. Sci. Lett.*, *48*, 363–370, doi:10.1016/0012–821X(80)902009.

Varet, J., and F. Gasse (1978), *Notice de la carte Geologique de l Afar du sud est*, CNRS, Paris.

Vigier, N., B. Bourdon, J.-L. Joron, and C. J. Allègre (1999), U-decay series and trace element systematics in the 1978 eruption of Ardoukôba, Asal Rift: Timescale of magma crystallization, *Earth Planet. Sci. Lett.*, *174*, 81–97.

Vigny, C., J.-B. de Chabalier, J.-C. Ruegg, P. Huchon, K. L. Feigl, R. Cattin, L. Asfaw, and K. Kynbari (2007), Twenty-five years of geodetic measurements along the Tadjoura-Asal rift system, Djibouti, East Africa, *J. Geophys. Res.*, *112*, B06410, doi:10.1029/2004JB003230.

Walter, M. J. (1998), Melting of garnet peridotite and the origin of komatiite and depleted lithosphere, *J. Petrol.*, *39*, 29–60.

Wang, K., T. Plank, J. D. Walker, and E. I. Smith (2002), A mantle melting profile across the Basin and Range, SW USA, *J. Geophys. Res.*, *107*(B1), 2017, doi:10.1029/2001JB000209.

Weaver, J., and C. Langmuir (1990), Calculation of phase equilibrium in mineral-melt systems, *Comput. Geosci.*, *16*, 1–19.

White, R., and D. McKenzie (1989), Magmatism at rift zones—The generation of volcanic continental margins and flood basalts, *J. Geophys. Res.*, *94*, 7685–7729.